Norwegian University of Life Sciences
Faculty of Environmental Science and Technology
Department of Mathematical Sciences and Technology

Master Thesis 2015
30 credits

Differences in N- and P-type mc-Si Characterized by Hyperspectral Imaging and EBSD Scans

Audun Ingebrigtsen

Acknowledgements

This master thesis is part of an on-going research project with the use of hyperspectral imaging on crystalline silicon for solar cell applications. The work in this thesis was carried out at the Department of Mathematical Sciences and Technology and Faculty of Environmental Science and Technology at the Norwegian University of Life Sciences (NMBU) and at Norwegian University of Science and Technology (NTNU).

First I wish to express my appreciation for the assistance my supervisors provided, Associate Professor Ingunn Burud, Associate Professor Espen Olsen and Senior Engineer Andreas Svarstad Flø. I have appreciated our weekly meetings with rest of the master students writing for Espen or related to solar energy. I want to thank Ingunn for all advice, proof reading and motivation. Espen, thank to all help regarding the solar cell and material physics. I also want to thank Associate professor Marisa Di Sabatino and Postdoctoral Fellow Chiara Modanese for their help and hospitality during my two weeks stay in Trondheim at NTNU, for parts of the experiments carried out for this master thesis. They worked as a partner in this research project and have provided the wafers used. At last I want to thank my family for support and my father for proof reading at the very end of this thesis.

With this thesis I end five year as a student her at the municipality Ås and conclude my master's degree in Environmental Physics and Renewable energy at Norwegian University of Life Sciences (NMBU).

Audun Ingebrigtsen
Ås, May 15th, 2015

Abstract

Characterization of solar cell materials is an important step towards changes in the production processes which will lead to higher energy conversion efficiencies. Firstly, the methods used in this study allows mapping of the crystallographic orientation on the samples surface. Secondly, it allows a correlation between the crystallographic mapping to defect related luminescence (DRL) caused by radiative Shockley-Read-Hall (SRH) recombination. Thirdly, it allowed a comparison on DRL between N- and P-type mc-Si wafers.

This experiment contained 5 unpassivated (125 x 125) mm^2 mc-Si wafers, from three different ingots, produced in a pilot-scale furnace. In two of these (N- and P-type) Fe contamination was achieved by adding about 50 ppmw to the silicon feedstock. The wafer from the last ingot were a P-type reference. In the hyperspectral analysis the wafers were cooled down to 90 K, then irradiated with a 808 nm laser and the excited photons are detected with a SWIR (900-2500 nm) hyperspectral camera. The detected photons are caused by band-to-band photoluminescence (BB-PL) and DRL. In the Electron Backscatter diffraction (EBSD) scans, the wafers were cut, ground, polished and then put inside a scanning electron microscope (SEM). There a thin electron beam irradiate the sample which causes high energetic backscattered electrons (BSE) to emit and hit a fluorescent screen where electron backscattering patterns (EBSPs) are recorded by the detector. Multivariate Curve Resolution (MCR) was used for statistical analysis, to split up recorded the emission spectra into different defect related spectra.

In the study of the hyperspectral images the key findings are: The apparent absence of both D3 and D4 at the bottom of the ingot in the N-type Fe contaminated wafer. A weak D4-band for a N-type wafer high up in ingot. For both N-type wafers (from the bottom and high up in the ingot), there were an apparent absence or very weak signal for D3, but instead presence of strong VID3.

This study is the first attempt to examine how EBSD scans could correlate with images produced from hyperspectral imaging. Different forms and contours present in both the EBSD scan and the corresponding hyperspectral image were found. A broad signal with peak around 0.7 eV in the reference P-type wafer seems to correlate with where different crystallographic orientations meet. For a Fe contaminated P-type wafer one crystallographic direction appeared to match the PL-image for D2.

Contents

List of Figures

Abbreviations

BB	**B**and to **B**and
BSE	**B**ack**S**cattered **E**lectrons
CI	**C**onfidence **I**ndex
CL	**C**athodo**L**uminescence
CSL	**C**oincidence **S**ite **L**attice
CZ	**Cz**ochralski
DFC	**D**ynamic **F**o**C**us
DRL	**D**efect **R**elated **L**uminescence
EBSD	**E**lectron **B**ack **S**catter **D**iffraction
EL	**E**lectro**L**uminescence
eV	**e**lectron**V**olt
HgCdTe	Mercury Cadmium Telluride
MCR	**M**ultivariate **C**urve **R**esolution
ALS	**A**lternating **L**east **S**quare
MG-Si	**M**etallurgical **G**rade-**Si**licon
mc-Si	**m**ulti**c**rystalline-**Si**licon
OIM	**O**rientation **I**maging **M**icroscopy
PL	**P**hoto **L**uminescence
SE	**S**econdary **E**lectron
SEM	**S**canning **E**lectron **M**icroscope
SOG-Si	**SO**lar **G**rade-**Si**licon

SRH	**S**hockley-**R**ead-**H**all
SWIR	**S**hort**W**ave **I**nfra**R**ed
TCS	**T**ri-**C**hloro**S**ilane
VID3	**V**ery **I**ntense **D3**

Chapter 1

Introduction

Every decade we postpone the emission reduction of CO_2 will lead to a 0.25 °C rise of temperature in 2100 [11], thus the more we reduce our carbon footprint the better. The energy situation in the world has for some time been faced with a transition from fossil fuels to renewable energies. This transition have been promoted and opposed from different sectors. Countries such as Germany and Denmark have been in the forefront with investments and framework conditions to promote a shift from dependence of fossil fuels to renewables.

Fossil fuels are, as know, non-renewable and thus will sooner or later, not be available to fulfill the worlds energy demands. However, there are many other reasons to encourage the use of renewable energies. Such are, reduction in carbon emissions and other types of pollution associated with exploration, production and use of fossil fuels. Oil spills and the vast areas devastated in Canada from the tar-sands exploration are other. The fossil fuels have in many countries lead to big profits in the pockets of only a handful of the population and the latest climate reports from IPCC predicts more extreme weather and many other negative changes regarding the climate. Which, are caused by the huge amounts of carbon emissions polluted by the human kind.

The renewable energies have for a long time been either to expensive to compete against fossil fuels or not accessible. Hydro power is one of few renewable energy which for many decades have been succesfully used for energy production at a competitive cost. Unfortunatly, this technology is not as accessible in many countries as it has been in Norway. Now, in the later years, several different renewable energies have been installed with an accelerated pace. As a result onshore and offshore wind, solar cells, solar thermal, geothermal and other technologies have come down to a levelized cost of energy which can compete with fossil fuels. In several countries the installation of solar cell modules are a good investment.

The sun illuminate our planet with inconceivable amounts of energy, 4 Yotta Joules every year. Which is, ten thousands times the energy consumption of the world in 2007 [15]. Thus, the sunlight can technically sustain all current and future energy needs. With solar cells with an efficiency of 10 %, only 0.1 % of the earths surface needs to be covered [13, 14]. However, the picture is a bit more complicated. Solar energy is a very diffuse energy source, most technologies produce power only during the day and have a significantly reduction with the presence of clouds. Further, the production of solar modules are capital intensive. Therefor, it is important to increase the efficiencies to the solar cells in order to further reduce the investment costs. Which, reduces the payback time.

Multicrystalline silicon is the most dominant material used for solar cells. Even tough monocrystalline silicon solar cells have a 2 % higher efficiency [7], multicrystalline silicon solar cells have lower process costs. The cause of the efficiency reduction are due to impurities and crystal effects. The lastest years the interest in understanding how impurities and crystal defects affect

the electrical properties of solar cells have increased. The key to improve the efficiency of multicrystalline silicon lies in understanding the effects of impurities, defects, how they interact and how these can be reduced, controlled or removed by changes in the production process of the material [7]. For a positive doped multicrystalline wafer, the presence of iron is considered to be one of the most deteriorating impurities [24].

The utilization of hyperspectral imaging on multicrystalline materials is quite new and it is developed at the Norwegian University of Life Sciences. However, the hyperspectral imaging as a technique together with statistical analysis is not new and well understood. From earlier master thesis's and one PhD the characterization of multicrystalline solar cells with the use of hyperspectral imaging have proven to give interesting results and is a valuable contribution to the great variation of different characterization techniques used for silicon materials.

This thesis deals with scans of unpassivated multicrystalline N- and P-type wafers. These scans, were recorded using hyperspectral imaging and a scanning electron microscope (SEM) with and electron backscatter diffraction detector (EBSD). The hyperspectral scans captures photoluminescence (PL) for many spectra. These were analyzed using Multivariate Curve Resolution Alternating Least Squares (MCR-ALS) and manual selection of emission signals. The EBSD scans wee analyzed using Orientation Imageing Microsopy (OIM) and these were compared with the correlated hyperspectral scans. A comparison between EBSD scans and PL scans from a hyperspectral camera has until now not been studied and this master thesis is the first attempt to investigate if there are any correlation. Together these two techniques can give valuable information as to what causes defect related luminescence (DRL).

The study of this thesis tries to find any differences in N-type and P-type wafers and tries to find any correlation between EBSD scan and hyperspectral imaging. The questions asked are:

- **What emission signals from N-type and P-type differ?**
- **Will the differences in N-type and P-type wafers change based on where in the ingot they are cut?**
- **How does these differences between N- and P-type correspond to the literature?**
- **Will the use of a macro lens reveal different PL-distributions than with a normal lens?**

This thesis is built up by 5 different chapters with this being the first. Next is a theoretical background chapter, then comes how the experiments were conducted, as chapter two and three respectively. Chapter four presents the results and discussion and the last chapter, number five, a conclusion and further research suggested. In the back matter, all the hyperspectral images and EBSD scans are presented.

Chapter 2

Theory

In this study the experiments were primarily conducted on multicrystalline n- and p-type wafers, plus one monocrystalline wafer and these were not passivated ("as-cut"). This chapter will therefore only have a brief introduction to how solar cells work and then focus on the properties of n- and p-type wafers and how they are produced, plus the effect of impurities (iron in particular) and luminescence.

2.1 A short introduction to solar cell physics

Semiconductors is by far the most dominant technology used to produce solar cells. The characteristic properties for a semiconductor, is a relatively narrow energy gap, ranging between a fraction of an electron volt to a few electron volts. The formation of an electron-hole pair is generated when an incoming photon excites an electron from the valence band in to the conduction band. This formation has the effect that parts of the photon energy is practically stored in the electron-hole pair. The pn-junction, created by a p- and n-type material, separates the electrons and holes generated by the electron-hole pairs and causes an external electric current to flow [4].

2.2 Production of Silicon Solar Cells

In order to end up with finished solar-cell modules, it takes several production steps. Broadly these can be split up in five main categories: (1) metallurgical silicon needs is produced, which facilitates as a raw material for (2) poly-crystalline silicon, which is used to the (3) growth of single- or multi-crystalline silicon ingots and ultimately is cut up in wafers. Then through solid state diffusion which introduce dopants and many other steps to produce finished (4) solar cells, these can then be connected together in a (5) solar cell module. The last step (5) is out of the scope of this thesis and will not be described [29].

2.2.1 Metallurgical-grad silicon

The raw material used to produce silicon solar cells, silica, is one of the most abundant on Earth. Silica also known as silicon dioxide, can be reduced by carbon and transformed to metallurgical-grade silicon (MG-Si), $SiO_2(s) + 2C(s) \longrightarrow Si(l) + 2CO(g)$ [15]. MG-Si has a purity on typically 98.5 %, good enough for use in e.g. steel and aluminum industries, but too low for use in solar cells [29]. A portion of the MG-Si is taken further to be used in solar applications. For solar-grade silicon (SOG-Si) a level of 4N (99.9999 %) purity or higher is required, however in order to produce high qualify solar cells, 6N or better is used [15].

2.2.2 Poly-Silicon

For the production of polycrystalline silicon, there exists two common used processes. In the Siemens process purifying MG-Si to highly pure polycrystalline silicon (9N) is done in three steps. In the first step silicon is converted to tri-chlorosilane ($HSiCl_3$ or TCS). This happens as hydrogen chloride (with copper as a catalyst) turns MG-Si into a fluidize bed of fine particles forming a range of chlorosilanes, including TCS. In the second step, due to TCS' low boiling point, it can be refined by fractional distillation. In the last step, at a temperature of 1150 °C the refined TCS is used to produce pure silicon by thermal decomposition.

The world's production of polycrystalline silicon is mostly generated through pyrolysis of TCS in the Siemens reactor (also called the bell reactor). In order to produce one batch of rods, it takes 24-35 hours and high amounts of energy [15, 29]. One byproduct from this process is silicon tetrachloride, earlier this was considered as waste. A newer method, developed by REC (Renewable Energy Corporation) uses the tetrachloride as a starting point. This new method is, according to REC, said to reduce the energy consumption significantly compared to the Siemens process [4].

2.2.3 Crystallization

In this step the goal is to produce thin wafers of silicon at a thickness of typically 200-350 μm. The most dominant wafering process for solar cells consist of a technique called directional solidification, carried out in a Bridgman type furnace. The feedstock for this process is normally the polysilicon produced as mentioned in Section 2.2.2 by the siemens process. In the industry Bridgman PV silicon ingots normally have a weight of 250 kg, but up to 650 kg and have a square cross-section. Most detrimental impurities are effectively removed during solidification, however the solid-state diffusion, results in a zone close to the crucible side wall and bottom. This zone have ineffectual electrical properties. This outer region is denoted as red zone, with iron as the major contaminant. Silicon crystallized in crucibles with low impurities have shown to have better electrical bulk properties and thinner red zone. Before the finished ingot are to be cut into vertical blocks and wafered by wire sawing, the red zone and top of the ingot is removed [2].

The predominant[1] wafering process consist of the Czochralski (CZ) process and produces large single crystalline silicon ingots (also called rods). This happens by a slowly pulling out a rotating crystal seed from a molten bath. The result is a crystal with the same crystallographic orientation as the seed pulled from the melt. For these rods, before they can be wafered, the crown (top) and tail (bottom) are removed and recycled as a feedstock to produce a new one. The finished wafer are dislocation-free, but will contain point defects and will take two days or more to produce a single silicon rod. An alternative to CZ process for the growth of single crystals is called float zone and has the advantage of very low levels of oxygen and high resistivity, however it has a higher cost [2, 29].

For both mono- and multicrystalline silicon suffer from large material losses due to sawing. These can exceed 50 % [2].

2.2.4 Solar cells

In a sequence of steps solar cells from silicon wafers are produced. First their optical and electrical properties are enhanced by chemicals (etching). The etching removes damages from the wafering process. Then a pn-junction is produced through doping of group 3 and 5 elements (typically boron and phosphorus), which creates an electrical field. Further, layers of anti-reflective coating

[1] The most dominant process of silicon for electronics

are added to reduce reflection losses by trapping incident light. In the last step, in order to complete the solar cell, electrical contacts are added on the front and back [15, 29].

2.3 Crystal structure & Defects in solar cell silicon

As seen in Fig. 2.1 matter in condensed state can take form in three different ways; crystalline solid, amorphous solid or as liquid. In the crystalline solid, the atoms is formed by an infinite repetition of an regular periodic array. It is the simplest possible way, matter can be formed. This is called a crystalline structure. When the position of one atom an its neighbors (called a basis or lattice) at one point in the crystal is known, the rest of the crystal is just a repeated stacking of the same lattice. This property is called long-range order and means that the locations of all atoms are known, just knowing the position of one given atom. In an amorphous solid the atoms are fixed as for a crystalline solid, but it does not form a regular array. Thus, for a given atom only the neighboring atom is known, this property is called short-range order. Liquids hold no rigid pattern, this implements neither long-range nor short-range order [22, 31].

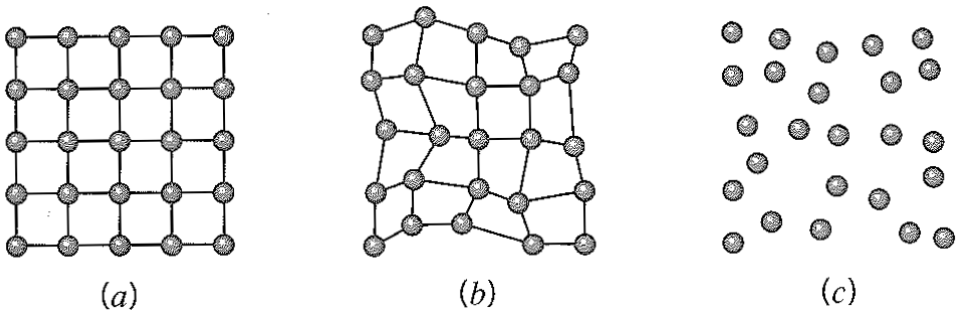

Fig. 2.1: (a) Crystalline solid, (b) amorphous solid and (c) liquid [31].

The the wafers used in this study is all multicrystalline silicon (mc-Si), therefor only the crystal structure of silicon is further explained. As mentioned the ideal crystalline material contains an infinite repetition of identical ordered and periodic arrangement of atoms. These identical arrangement may be viewed as a group of atoms and is called a basis. The lattice is a set of mathematical constructed points to which the basis is attached [15, 22], as shown in Fig. 2.1.

However, in the real world materials are rarely formed in an ideal way. For crystalline silicon, the atoms form tetrahedral covalent bonds with the four nearest neighbors, a diamond structure. There is a natural reason for why the crystalline silicon is formed this way; silicon lack four electrons in oder to fill up and get eight electrons in its valence shell (the octet rule). Thus, silicon can have an attractive interaction by sharing two electrons with another atom (e.g. silicon, phosphor and boron) [22]

The term multicrystalline silicon, tells us that the structure of the solid is made out of more than one crystal. In fact, several smaller crystals are formed in mc-Si and the result are more defects than for monocrystalline silicon made out of only one single crystal [20]. The added defects of a mc-Si solar-cell caused by the interaction between crystals results in a efficiency decrease of about 2 % compared to monocrystalline cells [7]. Defects in crystals can be categorized into four types: Point defects, line defects (dislocations), two-dimensional defects (surface defects) and volume defects [7, 21].

2.3.1 Point defects

For point defects there are two types: intrinsic and extrinsic defects. Intrinsic point defects can appear in pure metal. They are formed when there is an atom missing in the crystal (a vacancy), or the opposite, when the crystal have an interstitial atom. These two types are shown in Figure 2.2. Interstitial sites are relatively uncommon, but are high-energy defects. Vacancies, however, have a significant concentrations in all crystalline materials, governing solid state diffusion. Extrinsic point defects is either called solutes or impurities. Solutes, when intentionally added to the material, impurities if not. The foreign atom can either fill an interstitial site (interstitial) or occupy a lattice site (substitutional). Since interstitial sites are relatively small, larger atoms are usually found on lattice sites. Extrinsic point defects, as solutes, are of high importance because they are used to control electrical properties. Substitutional solutes are atoms that take place of one Si atom, during the doping process and are further explained in Section 2.6 [20, 21].

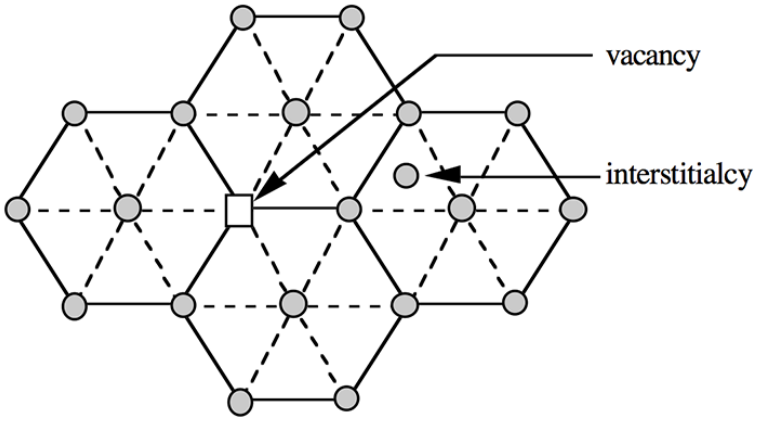

Fig. 2.2: The iIllustration displays a vacancy and an interstitialcy in a two-dimensional hexagonal lattice [21].

2.3.2 Dislocations

Line defects, also know as dislocations, are lines through the crystal. Line defects can be placed in two main categories: edge and screw dislocations. The occurrence of plastic deformation in crystals are caused by the motion of slip or twinning. A plane where slip occurs is called slip plane and is caused by dislocations. In slip, a considerable displacement for a unit of the crystal slides to a direction relatively to the neighboring units. For twinning, partial displacement occurs for slip on each of many neighboring crystallographic planes and are caused by surface defects [21, 22].

2.3.3 Surface defects

Just by visual inspection of wafers, interfaces between crystals such as grain boundaries and twins (also know as surface defects) can be identified, since they cause the separation of unequal crystallites. There are three categories of grain boundaries: coincidence site lattice (CSL) type boundaries, low-angle boundaries and random boundaries. These are divided by their degree of symmetry. For grain boundaries, 95 % is of some variation of the CSL type. However, other types of grain boundaries are more detrimental to electrical properties, as when the boundaries correlated with impurity decorations. Random grain boundaries generally have higher electrical activity than CSL boundaries, but have a very low density. Subgrain boundaries separates parts

of the crystal where the differences in orientation are very small and are formed during crystal growth or cooling. This is the most important grain boundary because its high densities compared with random boundaries and high electrical activity.

Even over small distances, the electrical activity for dislocations in multicrystalline silicon varies significantly. Both dislocations and grain boundaries causes an reduction of their energy and uncontaminated are not electrically active [7].

2.3.4 Volume defects

Three-dimensional defects (or volume defects) are changes in the crystal pattern over a finite volume. A common, but imprecise classification is based on the size and effect of the. The four categories are: precipitates, dispersants, inclusions and voids [21].

2.4 Energy band gap

All solids contain electrons. In crystals the wave functions of atoms interact and form energy bands, in which the electrons are arranged. Between these bands there are regions where no wavelike electron orbitals can exist. In theory the number of states of the energy bands is infinite, but the Pauli exclusion principle states that each quantum state only can hold one electron or each energy level can be occupied by not more than two electrons with opposite spin. At low temperatures, this implies that up to a certain energy level, all available states in the crystal is occupied by two electrons. This level is called the Fermi level, E_F an is illustrated in Fig. 2.3 [15, 22].

From the Fermi distribution it is shown that the temperature is a critical factor for semiconductors conductivity. At low temperatures, few electrons are free to move, thus low conductivity. At higher the temperatures, the electrons has a greater mobility, thus increased conductivity. In other words the temperature is a very important factor for the mobility of electrons and the recombination processes. Another even more important property, than temperature for semiconductors and their conductivity is the type of impurities [4].

A crystal can behave in three ways: as an insulator, metal or semiconductor. The determinants for how it behaves is the size and of the band gap and the highest occupied energy level (position of the band gap). The band gap (E_g) is defined as the difference in energy between the lowest (conduction band edge) and highest point (valence band edge) in the conduction band (E_c) and of the valence band (E_v), respectively. For semiconductors the band gap is relatively small, allowing electrons to be excited up from E_v to E_c.

For semiconductors there are two types of band gaps, direct and indirect. In a direct band gap, the lowest point of the valence band and the highest point of the conduction have the same momentum. For an indirect, as shown in Fig. 2.4 band gap the momentum is unequal. Silicon is an indirect band gap semiconductor. Thus the energy of a photon can be absorbed through two processes, by direct or indirect absorption [4, 15, 22]. The band gap can be measured in two particular ways. The first method is by electrical conductivity and is proportional with the number of electrons in the conduction band. The second is by optical absorptivity as a function of the frequency [17].

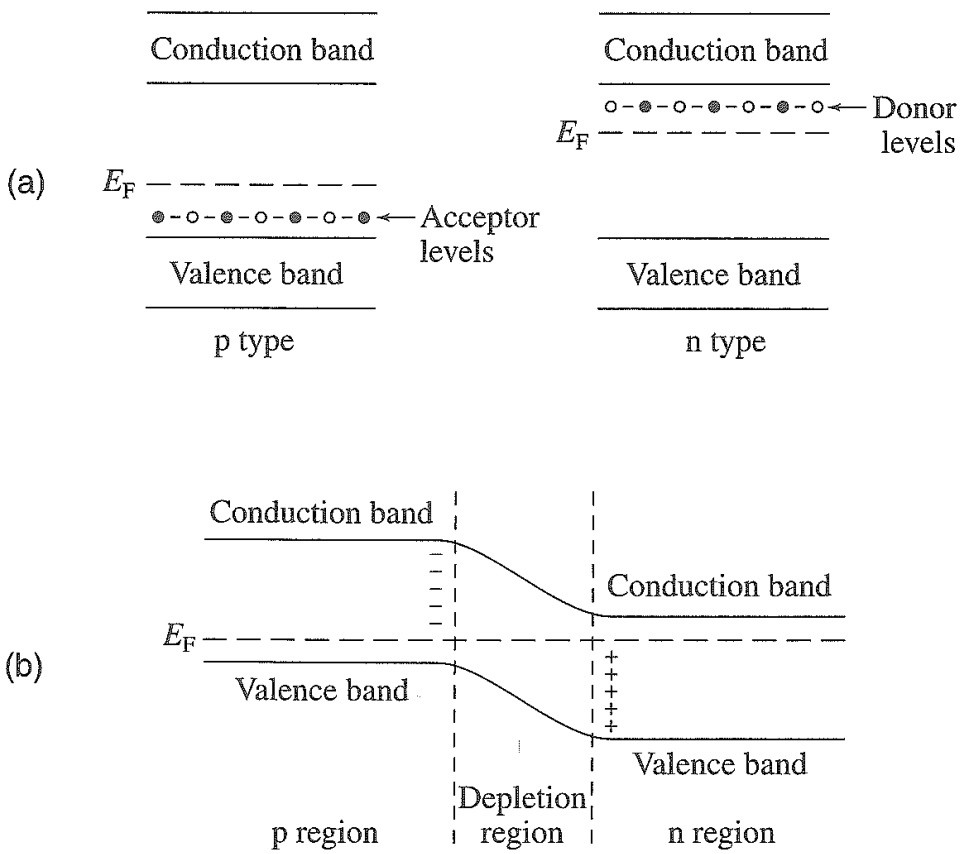

Fig. 2.3: (a) An energy-level diagram for an N-type semiconductor and a P-type semiconductor. (b) An energy-level diagram for when an N-type and a P-type semiconductor are in contact as a pn-junction [35].

2.5 Recombination

Just as different processes can generate electrons and holes, there also exist processes where they annihilate. It is called recombination when electrons and holes are annihilated. For this it is two main categories: radiative and non-radiative recombination. The trap-state recombination, however can result in both non-radiative and radiative recombination and is described in Section 2.5.3 [36].

2.5.1 Radiative recombination

Radiative recombination is the exactly reverse of when the absorption of a photon produces a electron-hole pair. A hole reacts with an electron and produces a photon. More precise it is when an electron from the conduction band transit to an unoccupied state in the valence band and the redundant energy is released as a photon. This mechanism for recombination across the energy gap is also called radiative band-to-band recombination (BB).

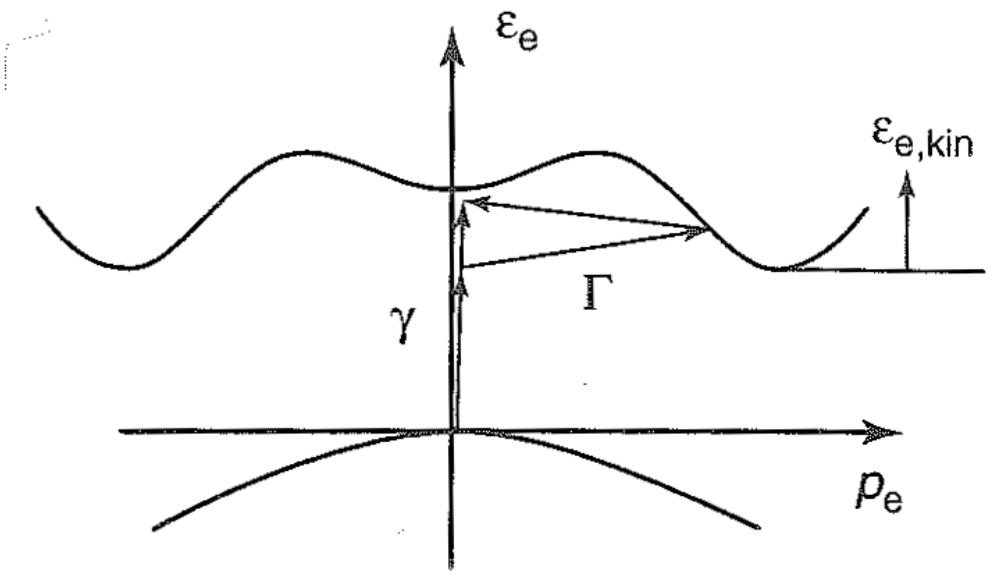

Fig. 2.4: Shows how the energy of electron states in the conduction and valence bands affect if it is a direct or indirect semiconductor. If the energy is not high enough to enter straight up, if it has momentum it can do a transition to the lower band gap to the right. [36].

2.5.2 Non-radiative recombination

Non-radiative recombination is caused by energies set free when electrons and holes recombine. These energies must be taken up by other particles and for non-radiative recombination these are electrons, holes or phonons.There are three types of non-radiative recombination: Auger recombination, surface recombination or impurity recombination [36].

Auger recombination

Auger recombination is an alternative process to radiative recombination. Instead of the emission of a photon with the energy E_g, this energy is transferred internally in the same band to a new electron or hole. A high kinetic energy to the electron or hole knocks another out of its band, thus creating a free electron or a free hole. The "extra" excited electron or hole loses its energy by thermalization (generation of phonons in collision with the lattice). The loss in efficiency from Auger recombination is unavoidable since it is an intrinsic process. Beside radiative recombination it is the dominant recombination process [4, 36].

Surface recombination

Surface recombination is a effect of a discontinuity in the crystal structure and causes a high concentration of surface states. These surface states appears when an large amount of the atoms at the surface are partially bonded. Each state can facilitate a two-step recombination, as a result a more-step recombination take place very easily (in stead of just two steps for trap-state recombination, explained in Section 2.5.3). The effect of surface recombination can be reduced considerably by passivation of the wafers [4, 30].

2.5.3 Trap-state recombination

Recombination caused by impurities is the predominant recombination process in real solar cells. The most important recombination from impurities is trap-state recombination, also known as Shockley-Read-Hall (SRH) recombination. Impurities and crystal defects can introduce electron states (traps) in the otherwise forbidden band gap. These traps can capture electrons and holes from a range of excited states and they are effective for the electrons to recombine through two steps, as shown in Fig. 2.5. In the process energy is released as photons or phonons. The activity of phonons are temperature dependent. Lower temperatures leads to a decrease in the phonon activity and the rate of radiative recombination through traps increases [15, 36]. M. Tajima et al. studied the emissions from the inter band gap and concluded that the signals appears as separate signals below 100K [34].

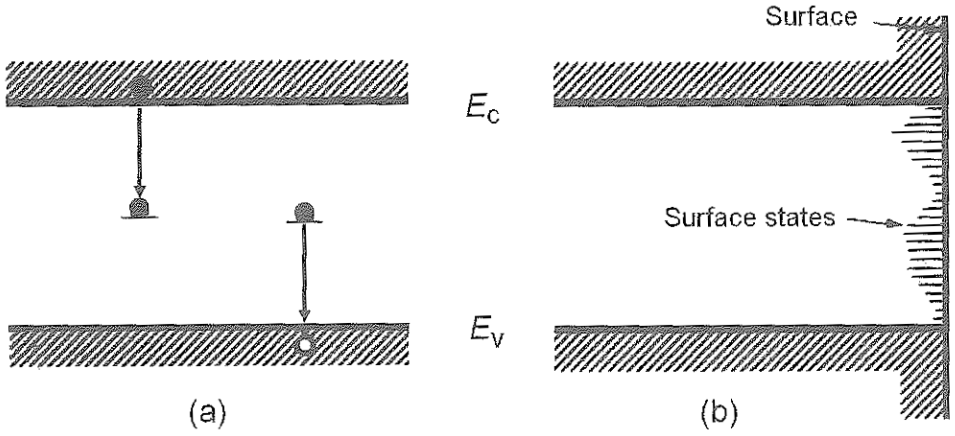

Fig. 2.5: (a) Show a trap-state recombination where a electron-hole pair can recombine and transfer energy E_g into either a free electron near the conduction band edge, E_c or free hole near the valence band edge, E_v (b). Then the excited electron or hole quickly loses its excess energy to the lattice as phonons. (b) Show that surface recombination can occur in many steps along the surface of the semiconductor, through several introduce energy levels. [4].

Impurity levels in the vicinity to the conduction or the valence band are less effective. Most of the time these levels are not occupied by electrons. More frequently, for impurity levels close to the conduction band, captured electrons are emitted back to the conduction band, rather than recombine with a hole captured from the valence band. For impurity levels close to the valence band more, they are most of the time occupied by electrons. Before a hole can recombine with a captured electron they emit back to the valence band. However, impurities that introduce energy levels near the middle of the band gap, generally degrades the efficiency of finished solar cells [36].

Thus, the impurities which introduce energy levels close to the conduction or valence band are acceptable in larger quantities than those introducing energy levels in the middle of the forbidden band gap. The emission of photons from recombination at different impurity levels and crystal imperfections causes luminescence with different unique energies [15]. These emissions are denoted Defect Related Luminescence (DRL).

2.6 Doping

Doping is a process where a controlled amount of impurities is added to a semiconductor material. These impurities enters the crystal structure and change the electron budget of the material.

The impurities simply take the lattice position of an atoms in the crystalline silicon. The conductivity in the silicon material is highly affected by the concentration of impurities [4, 36]. However there are certain impurities and imperfections in crystalline silicon which drastically affect the electrical properties. An example is the addition of boron to silicon, where 1 boron atom to 10^5 silicon atoms increases the conductivity of pure silicon by a factor thousand at room temperature [22].

2.6.1 N-type

For a n-type (n for negative) doped silicon wafer, the impurity atoms have more valence electrons than is necessary for chemical bonding. In most cases it is only one extra outer electron, which means five outer electrons. Such impurities are also denoted as donors. Atoms from group V in the periodic table, such as N, P, As and Sb are effective donors, all with on extra outer electron. The donors results in a shift for the Fermi level towards the conduction band. Phosphorus is a good candidate and often used for doping in a n-type semiconductor. Because of the additional positive charge on the phosphorus nucleus, the extra electron in phosphorus is more attracted to it's "mother" than to silicon atom. However the binding is not in particular strong, with an energy of 0.05 eV. Which means, to dislodge and push the extra electron into the conduction band, it takes relatively little energy.

2.6.2 P-type

For a p-type (p for positive) doped silicon wafer, the impurity atoms have one valence electron less than necessary for chemical bonding with the neighbouring atoms, than for silicon with its four. Such impurities are also denoted as acceptor. Atoms from Group IIIB in the periodic table such as B, Al, Ga and In are effective acceptors. The acceptors results in a shift for the Fermi level towards the valence band. Boron is a good candidate and often used for doping in a p-type semiconductor. With with typically only 0.05 eV, boron can borrow an electron from a silicon atom. This gives boron the ability to form a requisite covalent bond with neighboring silicon atoms and by it introducing empty energy levels just above the valence band [35, 36].

2.7 Luminescence

There exists three different causes for when luminescence from silicon that can occur. First, when electrons are excited by an electric current, know as electroluminescence (EL). Second, when electrons are excited by an electron beam, known as cathodoluminescence (CL). Third, when electrons are excited by photons, known as photoluminescence (PL). By definition, PL is when light is emitted from a material after the absorption of photons. The emissions are caused by energy exchange within the material and as explained in Section 2.5 these emission is a result from either BB and SRH recombination. A PL spectrum can be used to determine the electronic energy levels through the transition energies it provides [12]. Usually surface recombination is non-radiative and reduces the band-to-band photoluminescence intensity. A laser functions well as an excitation source for PL [9].

2.8 Defect Related Luminescence

There exists several radiative emission mechanisms in silicon other than the wanted band-to-band recombination and trap-state recombination. In 1976, Drozdow et al. [8] reported four radiative emissions lines believed to originate from recombination related to dislocations in the crystals.

These lines had the energies 0.8 eV, 0.87 eV, 0.94 eV and 1.0 eV and were labeled D1, D2, D3 and D4, respectively.

Through the years several theories have been proposed for the origins of the D-lines and other emissions related to Defect Related Luminescence (DRL). One theory proposed by Sauer et al. [32], suggested that D1-D4 are due to relaxed dislocations, another is from Higgs et al. [18] that believed the source for the D-band emission lines are transition-metals. It is also believed that oxygen or heavy metals have an impact on the half-width and intensity of D1 [28]. D3 and D4 has been associated with slip lines, D1 and D2 has been linked to intersections of plural slip. Further regarding the spatial distribution between D1/D2 and D3/D4 a pairwise similarity have been observed [33]. Moreover, Arguirov [1] have proposed that D3 and D4 are linked to dislocations decorated by metallic impurities. Brown and Hall [3] have attributed a strong emission line at 0.93-0.94 eV, different from D3 and the signal has been related to dislocation network formed at $\Sigma 3$ grain boundaries [23]. This strong emission line is called very intense D3 (VID3) and have later been identified to have a wider range, 0.92-0.96 eV [26]. Besides, Flø et al. reports a broad signal peak at 0.75–0.76 eV, separated from another broad peak at 0.68 eV, plus a peak at 0.7 eV. These peaks are believed to be caused by point defects and showed to be mainly located at grain boundaries [9].

2.9 Iron

The presence of iron in p-type mc-Si is rated as one of the most common and harmful impurities for use in solar cells [24]. Further, for a p-type iron-contaminated ingot, it is not expected any strong contamination of other impurities. As a fast diffusing impurity in silicon, iron introduce allowed traps close to the middle of the band gap, thus reducing the carrier lifetime in mc-Si ingots dramatically by introducing recombination centers [7, 24]. Sources for the contamination of iron are feedstock and furnace environment, surfaces in direct contact with the melt or solidified silicon.

Later iron is also introduces during emitter diffusion and firing of contacts. The concentrations reported from commercial mc-Si ingots are well above the levels where interstitial iron could drastically reduce the performance of the solar cell. In silicon, iron has a low distribution coefficient and most of the iron will accumulated in the liquid phase during crystal growth. However, due to a high diffusivity i solid silicon and by slow cooling from high temperatures, the accumulated iron at the top will diffuse back into the bulk [24].

Chapter 3

Experimental Setup & Data Processing

This chapter describes the different experimental setups and the data processing performed on the recorded images. Two different characterization methods, EBSD and hyperspectral imaging, were used in experiments conducted for this master thesis. First the wafers used for both these two methods will be described, then most of the details regarding hyperspectral imaging. Then principles for EBSD and the details for how the samples were prepared and the scans were carried out.

3.1 The Wafer Samples

The wafers used in this study are displayed in Fig. 3.1. The wafers except (f), are from a work in a previously published study done by Kvande et. al (2008). Further, these are multicrystalline, were cut from a 12 kg ingot[2] and made in a pilot-scale furnace[3] by directional solidification at SINTEF/NTNU. The multicrystalline wafers were cut to a thickness of 240 μm [24]. The last wafer (f) is produced by Norsun. In the wafers labeled with FS6 and FS7 the Fe contamination was achieved by adding about 50 ppmw to the silicon feedstock. The wafers are divided into two groups, one of P-type and the other of N-type, as indicated in Fig. 3.1. Both the P-type and the N-type wafers have one reference-wafer each. FS8-015 for the P-type wafers and a monocrystalline from Norsun for the N-type wafers. Common to all of the wafers is that they are "as-cut" and neither are passivated.

Unlike what Fig. 3.1 seems to show, the wafers are equal in size, 12.5 x 12.5 cm. The reason why they are not equal in size on the figure is that they have been photographed with a mobile phone camera (Samsung Galaxy k zoom) and not directly from above. After that the pictures have been cropped and the perspective distorted to make them square. Since the wafers got cut in several pieces as a part of the preparation for the EBSD scan, a new and proper picture was not possible. Lighter and darker areas are due to lighting conditions. The horizontal line a cross (f), it is actually not on the wafer but is due to lighting conditions and reflection in the wafer from something in the room the picture was taken.

[2]The dimensions of the ingot were a diameter of 250 mm and a height of 110 mm.

[3]Crystalox DS 250. Designed to be representative of the mc-Si ingots solidified by the industry, the furnace has been extensively studied [24].

(a) FS6-015, P-type with Fe **(b)** FS6-031, P-type with Fe **(c)** FS8-015, P-type reference

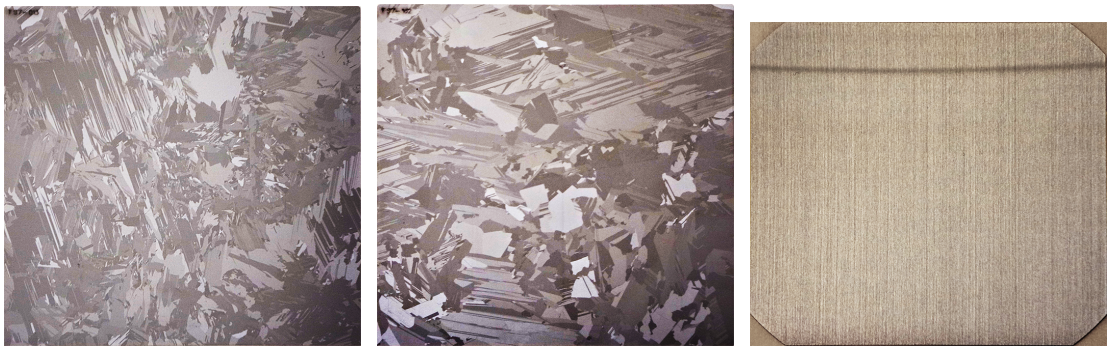

(d) FS7-013, N-type with Fe **(e)** FS7-162, N-type with Fe **(f)** Norsun, N-type reference

Fig. 3.1: Solar cell wafers used in this thesis. The first and second row is respectively P-type and N-type solar cells.

3.2 Hyperspectral Imaging

This section describes the experimental setup of the work that has been done with hyperspectral imaging in this master thesis. The full wafer scans were done the 1st of February 2015 and the macro pictures were done the 17th of February the same year. The different parts of the experimental setup, seen in Fig. 3.2, are also thoroughly explained.

3.2.1 Experimental setup

The setup for the hyperspectral imaging as seen in Fig. 3.2 is placed in a black steel-frame, inside of the steel-frame a black plate serves as a table. All the sides around the setup are or can be covered by black cloth and plates to protect from any incoming light. When the measurements are done the light is turned off, the outer doors to the room closed, the only light source in the room is a LED computer screen. The plates and cloth around the frame insures that no other light than the illumination from the laser is present on the wafer. In this way we have a controlled setup where we know the energy illuminated on the sample.

More about the different parts of the setup follows in separate sections about the instrumentation.

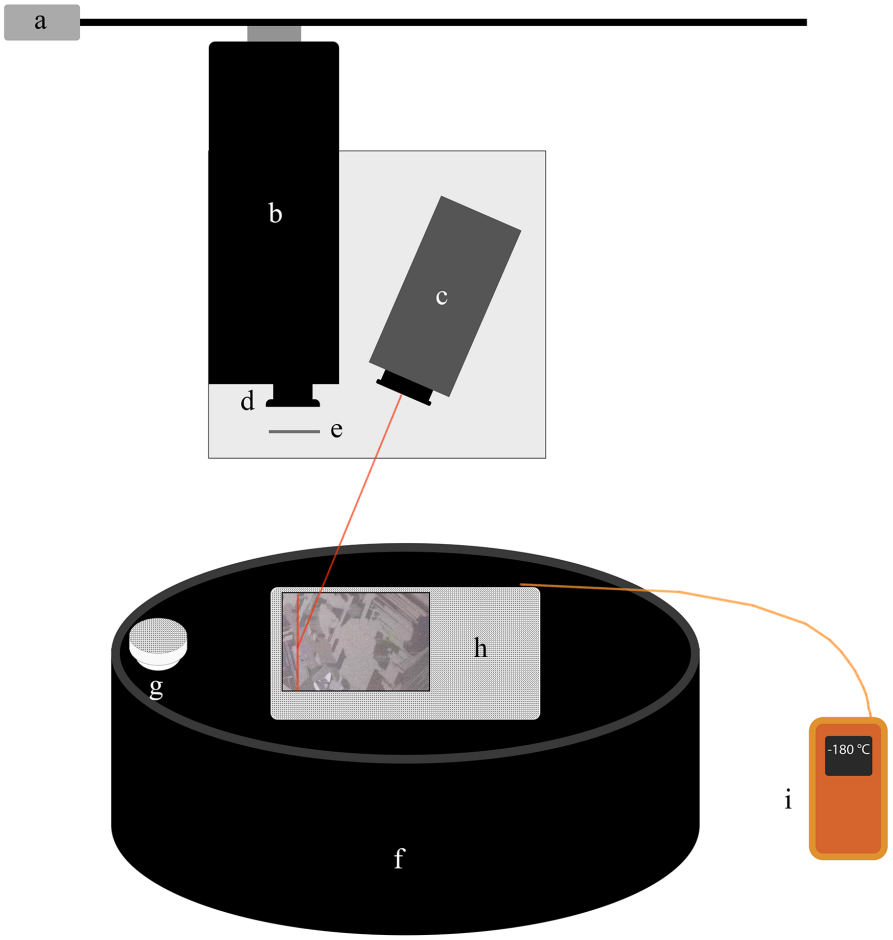

Fig. 3.2: The hyperspectral imaging setup consist of (a) one-axis movable rig, (b) hyperspectral camera, (c) laser beam for illumination, (d) objective lens, (e) longpass filter, (f) cryogenic cooler, (g) inlet for liquid nitrogen, (h) sample holder with sample (for illustration of use) and (i) thermometer

3.2.2 Movable rig

Fig. 3.2 (a) displays a translation stage (electric driven motor) that is controlled by an application[4] provided by the manufacturer. The rig is movable along one axis, that is in left-right-direction as seen on the figure. This is what makes the y-axis on the images recorded by the hyperspectral camera. Through the application that controls the recording of the pictures, settings as scanning speed, retrace speed and scanning length can be set. The grey area behind the laser and the camera in Fig. 3.2 is a steel plate mounted to the translation stage. The laser and the camera are attached to this plate. This ensures that both the camera and the laser moves at the same speed at the same time.

3.2.3 Laser

The laser used in the hyperspectral setup, seen in Fig. 3.2 (c), is a 808 nm, 5 W line laser. It goes by the name Lasiris Magnum II and is produced by Gammadata Instrument AB in Upp-

[4]Spectral DAQ, Specim, Version 3.62.191.24-R

sala, Sweden. The laser provides a irradiated power density of 2 W/cm^2, it does not provide a absolute flat profile as earlier thought [9], a simple study done by master student [37] showed how the profile varies along the x-axis, see Appendix A. The voltage provided to the laser was set to 5 Volts.

3.2.4 Hyperspectral measurement

When a recording with a normal camera is done, it captures an image in two dimensions and each pixel records intensities for red, green and blue. A hyperspectral camera also captures a two-dimensional picture (spatial resolution), but instead of recording one single value for red, green and blue in each pixel, it records values representing a set of different intervals of wavelengths, thus creating a third dimension. Values from each interval have can generate a correlated spectral image. The camera's ability to capture several spectral images in one recording, implies it is a hyperspectral camera[5].

The camera used to record Hyperspectral images, seen as (b) in Fig. 3.2, is a HgCdTe SWIR produced by the company Specim (Spectral Imaging Ltd.) located in Oulu, Finland. It captures an image by scanning on line at a time, where each line is captured as a two-dimensional picture; spatial (x-position) and spectral (z-position). The spatial resolution is 1 x 320 pixels. Thanks to a prism inside the camera it is possible, for each pixel in the spatial resolution, to split up incoming light and send it to 256 different sensors. Each sensor records a unique band of wavelengths. All together the bands records approximately in the range of 900–2500 nm. Thus each line captured by the camera has a resolution of 320 x 256 pixels.

Settings selected on the camera has been done through the same computer program that controls the movable rig. For every hyperspectral recording in this thesis the frame rate has been set to 25 Hz and the exposure time to 20.0 ms. AutoDark is a part at the end of the recording where the shutter is closed, this section is later used to remove noise caused by the sensors inside the camera and was set to 3000 ms. A consequence of the latter, the AutoDarkStartline (where the AutoDark starts) were automatically set by the program to be at respectively 368 ms and 4322 ms for the recordings done with the focusable[6] and with the macro[7] lens.

The resolution to the recordings done with the normal and macro lens is respectively 2 pixels/mm and 33.33 pixels/mm. Thus, scanning over the 12.5 cm long wafers the camera can record 250 and 4167 pixels with the normal an macro lens respectively.

To prevent second harmonics at 1616 nm from the laser in the recorded image, a 850 nm High Performance Longpass Filter (Edmund Optics Inc., NJ, USA) was used. The filter was taped in front of the camera lens, since the research group did not have any filter that can be mounted.

To be sure the recordings were in focus, the computer application provided to scan continuously was used. Without the filter, illuminated by normal lighting, the focusing could be done through the focusing ring on the normal lens. The macro lens on the other hand had no focusing ring, so the focus was adjusted by changing the distance between the lens and the sample. Placing different numbers of magazines and paper sheets under the cryogenic cooler were how the distance was adjusted in this study.

For each wafer using the normal lens, three recordings were taken immediately after another.

[5]Valid for more than ten spectral images, in the range between two and ten spectral images, it is called a multispectral camera

[6]OLES30, focal length: 30.7 mm, f/2.0, spatial image size: 12.8 mm

[7]OLESMacro, focal length: 73.3 mm, f/4.0, spatial image size: 10.0 mm

From these three a median picture was produced using MATLAB. In this way an error that might occur in only one of the three measurements will be corrected from values from the other two. With the macro lens only one recording was done for each sample, due to the big file size generated for a single recording.

3.2.5 Temperature controller

Since the radiative recombination through traps increases with lower temperatures, cooling of the wafers is necessary to properly detect DRL. In order to cool the samples a cryogenic cooler as seen in Fig. 3.2 (f)[8] and a thermometer (i)[9] is used to control the temperature. The cooler is the third version produced for this purpose at IMT, NMBU. The cryogenic cooler as seen as (f) in Fig. 3.2 is a steel container with a part of it (h) made out of aluminum. The aluminum piece is in direct contact with the liquid nitrogen through cooling fins. The black parts on the cryogenic cooler is the 5 cm thick isolation of styrofoam that covers the steel container on the sides and bottom. On the top there is a separate isolation plate that is 2 cm thick.

In Fig. 3.2 (g) is a plug of styrofoam covering the opening where liquid nitrogen is to be poured into the steel container. Inside there is a liquid-lock, that keeps parts of the nitrogen outside the main cooling chamber. The liquid nitrogen outside the lock is free to evaporate, which it does at a temperature of 77 K and atmospheric pressure. The nitrogen gas is flowing out of the cooler through several small pinholes equally spread on each side of the sample holder (h). The main function of this is to prevent a layer of frost to develop on top of the sample.

To cool the cryogenic cooler down to temperature where the thermometer shows around 77 K (-180 ° C) around 11–12 liters of liquid nitrogen was used. Once cooled the wafers achieve a state of thermal equilibrium with the cooler within seconds, when placed on the sample holder. The thermometer measured the temperature on one of the screws connected to the steel container. It is located close to the sample holder, just above one of the pine holes.

3.3 EBSD Imaging

An advantage with the use of electrons as a "light"-source is it's wave length. Where an optical microscope uses light with wavelengths in the magnitude of several thousands Å, electrons accelerated through a potential on e.g. 30 kV achieves a wavelength on 0.07 Å. A determinant for the resolution of a microscope is the wavelength of the light source, the shorter the wavelength is, the higher the resolution gets. Thus, the use of accelerated electrons as "light" increases the resolution from optical microscopes significantly. A Scanning Electron Microscope (SEM) is such an instrument that uses accelerated electrons as light and is therefor a valuable instrument for characterization of heterogenous materials and surfaces on micro scale [19].

A thin electron beam, focused by magnetic lenses, irradiate the area to be examined. The electron beam is generated by a filament where electrons are emitted and then accelerated through a potential field in the range of 1–40 kV. The beam is either stationary or can scan in a raster over parts of the sample surface. Several types of signal can be detected when the beam of electrons hit the surface of the sample; low energetic electrons (secondary electrons – SE), high energetic electrons (backscattered electrons – BSE), characteristic and continuous x-rays, Auger electrons and photons with different energies. Through dedicated detectors this range of different signals can give information about different properties such as: the chemistry, topography or e.g.

[8] built by the technician Arne Svendsen at IMT, NMBU
[9] Fluke t3000 FC K-type thermometer

crystallography of the sample [19]. In order to analyze the crystallographic orientations of the samples in this study, the backscattered electrons were of interested.

If the tilt angle of the sample is increased, the electrons will propagate closer to the surface and amplify the probability for backscattering [19]. Therefore the samples in this study were tilted with 62° from the horizontal plane. In a crystalline sample the structure of the lattice has an impact on how the primary electrons interacts with the atoms near the surface. The primary electrons are those emitted from the electron beam. The atom structure behaves more open in certain crystallographic directions than others, and this causes a diffraction effect [19].

In order to generate an Electron Backscatter Diffraction (EBSD) image, recordings of a Electron backscattering pattern (EBSP) is needed. For this a stationary electron beam is used. Due to tilting between 60–80° the primary electrons are diffracted on their way out of the sample and form a characteristic pattern. This is then detected by a fluorescent screen [19]. From different sample regions, different characteristic diffraction patterns are generated. These patterns can provide information of the crystal structure and orientation in the sample region. Further it can provide information of the local crystalline perfection, crystal orientation and characterize grain boundaries. Through Orientation Imaging Microscopy (OIM) these diffraction patterns is used to obtain an image file with the mentioned information. The original images generated in this study are presented in Appendix B and Section 4.2.

A SEM together with an EBSD detector were used. The EM-lab (Electron microscope-lab) at the Institute for Material Technology (IMT), NTNU was used during the EBSD experiments in this thesis. In order to get images showing the crystallographic orientation on the surface of the sample the feature combo-scan was necessary. JEOL JSM-840A Scanning Electron Microscope (Tokyo, Japan) had this capability.

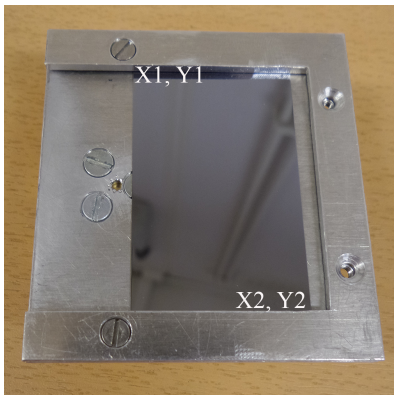

Fig. 3.3: The sample holder for the EBSD with a sample ready to be inserted into the SEM.

Fig. 3.3 shows the sample holder with one sample ready to be scanned and a picture of the SEM and EBSD is shown in Fig. 3.4. In Fig. 3.3 it is marked where the combo-scan starts and where it ends (X1,Y1 is where it starts and ends at X2,Y2). The edge where it starts is the original outer edge on the wafer before it was cut (The cutting procedure will be described in section 3.4.1). Due to space limitations inside the chamber to the SEM, it was not possible to scan the whole width of the sample. Due to a troublesome laser cutter, the width of the samples was not constant at 30 mm as wanted, but varied from 28 to 30 mm. Further the sample holder covers 8 mm of the wafer on the top and bottom to hold the wafer in a fixed position. So the upper and lower parts of the sample were unavailable for EBSD recording.

For the experiments done with the SEM a magnification of 70x, working distance of 30 mm and a tilt on the stage scan of 62° was set. To get a straight scan the stage had to be rotated, the rotation setting varied somewhat, but was set to around 198 on two of the scans and in the interval 277–285 on three other. The latter seemed to give the best results since these recordings produced no loss in information (black areas) on the long side of the samples. To get the best results (highest confidence interval (CI) possible) it was necessary to adjust the stigmator, adjust for wobble, and dynamic focus (DFC). The coordinates to where the scan where to start and end was done by navigating around on the sample with a joystick and then writing down the the numbers for X1, Y1, X2 and Y2.

By using the OIM Data Collection Application (EDAX) installed at the computer connected to the SEM through a MSC2000 (TSL/EDAX) the application was calibrated through a procedure until a CI above 0.60 was achieved, the resolution (step) was set to 150.00 microns (μm) and the final exact coordinates for the scan was set. Then the scans could be initiated and the result appeared some 4-6 hours later.

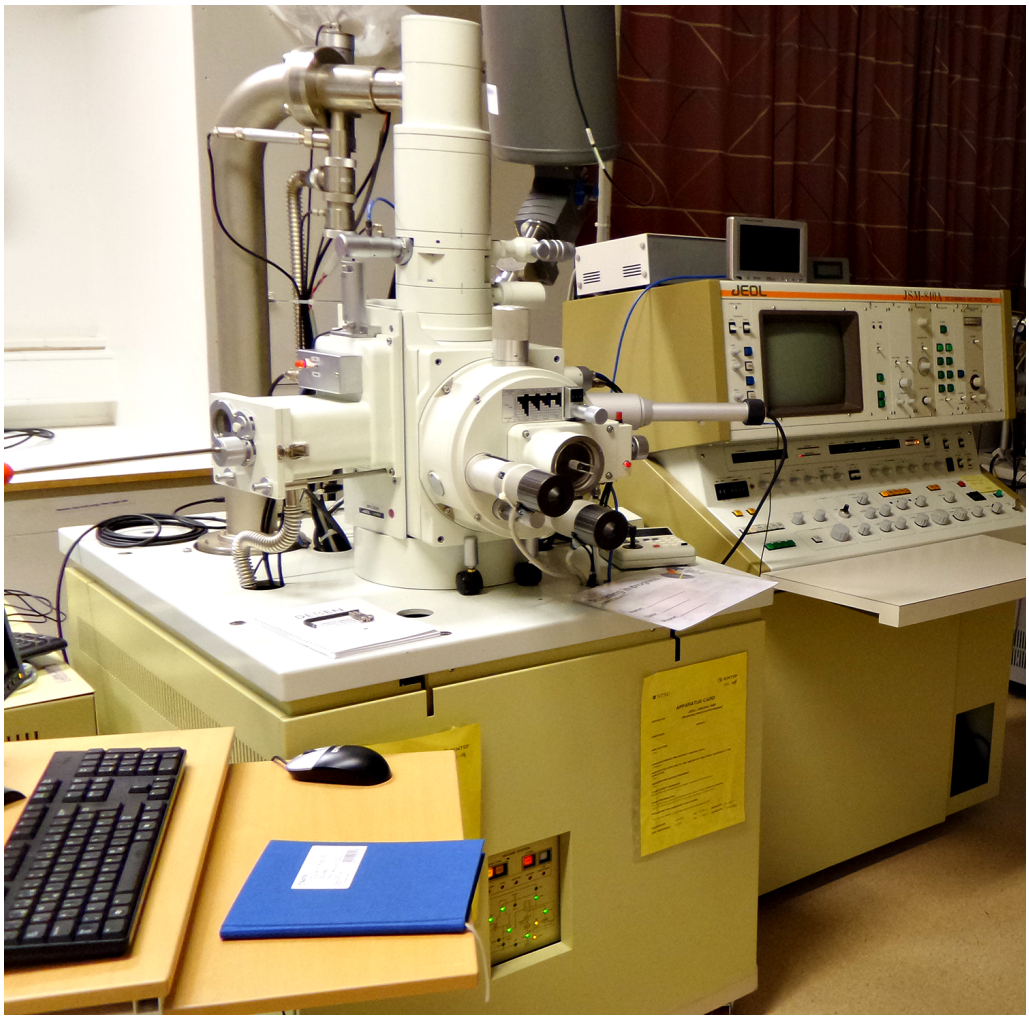

Fig. 3.4: The figure shows the SEM located at the EM-lab, NTNU. The chamber, with the SEM column, EBSD detector, stage control etc. is on the left and the analog controlling unit is on the right. The controlling unit was used for zoom, focus, power and some other parameters. For the navigating the stage a joystick unit was used and for the recording a computer with application, TSL OIM Data Collection (EDAX) was used.

3.4 Sample preparation for EBSD Imaging

Preparation of the samples is very important when the crystallographic orientation on the surface is to be studied with EBSD. First, there is an upper limit to the samples dimensions to be used inside the SEM. The limit is roughly (55 x 55 x 25) mm^3, for the samples used in this sample the

thickness is in itself not a problem, but since the sample is tilted to 62° this results in a width limit to approximately 26.4mm. Second, the contrast in the pattern is produced from the top 500 Å and 5 % of the backscattered electrons produced, this makes the signal very weak [19]. Therefor grinding and polishing is done to have the best possible basis.

3.4.1 Laser cutting

The original samples were (125 x 125) mm^2, this by far exceeds the limits to be examined using the SEM. A part of the samples had to be selected and cut out from the original wafer. A laser cutting machine from Stjernberg Automation (Kungsbacka, Sweden) was applied and the settings were made with Virtual Laser Marker and Visual Marking Controller VMC2 (Rofin, Germany).

First the samples were cut in two, where the smallest part was 125 mm long and between 28–30 mm wide. After the grinding and polishing process of the 125 mm x 28–30 mm part was cut in two parts again. Now there were to equal small parts on 62.5 mm x 28-30 mm, as illustrated in Fig. 3.5.

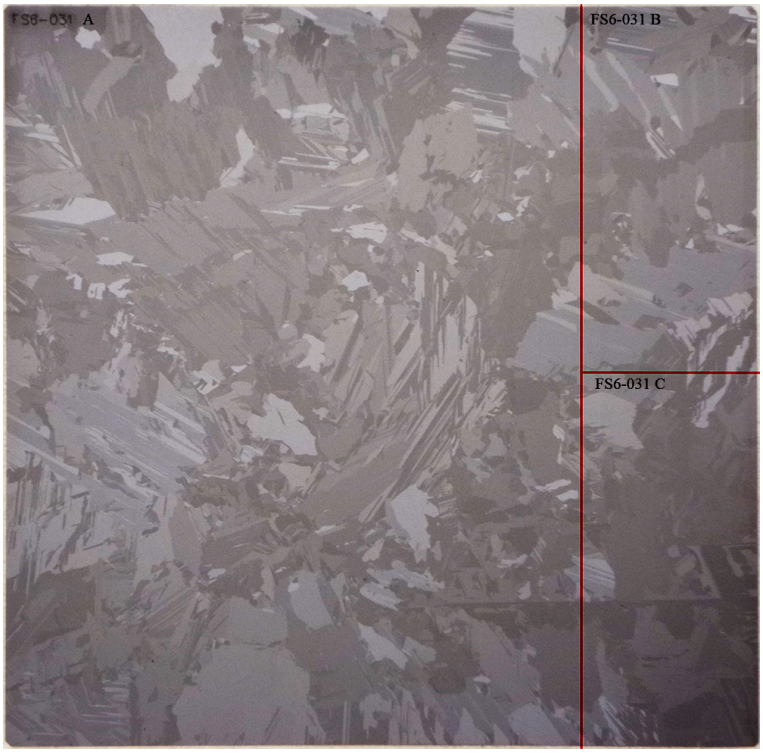

Fig. 3.5: The figure shows where the wafers were cut and how they were marked with a letter appending the wafer number.

3.4.2 Grinding & Polishing

The grinding and polishing process was done with Struers AbraPol-20, an automatic machine with a 350 mm disc (Ballerup, Danmark). First, before anything can be done, the samples needs to be fixated under a sample holder with wax. This is achieved by heating the sample holder until it is warm enough for the wax to melt, then the sample holder is put away. Now the wafer

is warmed (takes a few seconds) and wax is applied evenly on the wafer's back. Then the wafer is put aside on paper and the heated sample holder is put on top of the sample. It is important that the wax is evenly spread on the back of the wafer. Therefore circular movements is done with the sample holder, when the wafer is placed under it. For the wax to stiffen the sample has to dry for 1-3 hours before it is ready for the next step. A fixated wafer on the sample holder can be seen in Fig. 3.6.

The next step is grinding of the samples, this was done with 1200 FEPA[10] grit size SiC (Silicon Carbide) paper from Struers. The grinding was done only a few seconds, max 20 seconds. With some of the samples the grinding wasn't done uniformly on the wafer, to rectify this manual grinding was necessary. For this the author got help from the PhD-student Guilherme Gaspar and was done on an older machine, where the operator self applies the downward force.

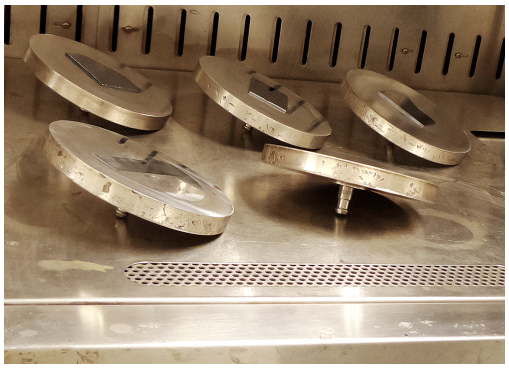

Fig. 3.6: Sample holders with samples for the grinding & polishing process. The upper three in this figure, is not part of this study.

The samples were now ready to be polished with 9, 3 and 1 μm cloths. The 9 and 3 μm cloths is of the MD-Mol type, but the 1 μm cloth is of the MD-Nap type. The cloths is produced by Struers. The polishing process lasted on each step 2–3 minutes. To remove the slurry produced between each of the steps, the samples were cleaned and gently wiped with wet paper under running water. The last step was to put the samples under hot running water until the wax melted and the samples could be removed from the sample holder. Then the wax on the wafer was removed with more hot running water and then set to dry.

3.5 Data Analysis

3.5.1 MATLAB

To process and analyze the data recorded using the hyperspectral camera MATLAB (R2014b) has been the prime software. The research group working on hyperspectral imaging has developed different scripts to be used when processing the images recorded. These scripts were used to subtract most of the systematic noise and errors from the camera. MATLAB has further been used to crop the images, so only the area of the wafer was used, to produce a median image when three recordings of the same sample were taken. Finally, MATLAB was applied to select specific waveband regions (e.g. DRL images) and to perform Multivariate Curve Resolution. The used scripts and code are presented in the Appendix C.

[10]The European FEPA (Federation of European Producers of Abrasives) is one of the two most common standards for the size of SiC particles, the other is the United States CAMI (Coated Abrasive Manufacturers Institute)

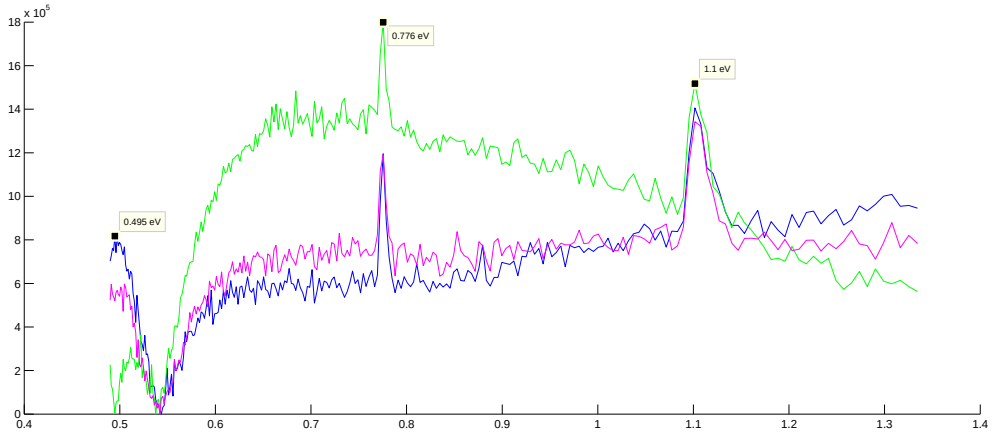

Fig. 3.7: A plot over the PL recorded through three different takes of the Norsun-wafer.

With the use of MATLAB a spectrum plot from the hyperspectral recordings can be presented. In this thesis three continues recordings of the same wafer has been undertaken. An example of how three spectrum recorded of the same wafer in three continuous takes can be presented, is shown in Fig. 3.7. Statistical analysis such as a Multivariate analysis (presented in Section 3.5.2) can be used to extract signals from these spectra and in this thesis MCR is used.

3.5.2 PLS & MIA Toolbox

PLS and MIA are two toolboxes for MATLAB developed by Eigenvector Inc. and can be used for analysis of hyperspectral imaging. These two combined have been used to load and perform a Multivariate Curve Resolution (MCR). For the recorded hyperspectral images, MCR is a powerful tool for quantitative analysis. Except the measured data matrix, the only input needed, is an estimate on how many components there are. This feature makes this analysis method in particular favorable, when no information about the data is available in advance. The PLS Toolbox uses a version of MCR called MCR-ALS. This is an iterative method that transforms mixed information and generates "pure" concentration profiles and spectra, through the use of a bi-linear model and a version of least squares method called Alternating Least Squares (ALS) [6]. Out of the analysis, a two-dimensional image with its relative concentration for each component is generated. Through statistical analysis the MCR is able to separate the signal from the images in different components even if they are spectrally imbricated and spatially coincident [16]. Each of these components represents ideally different unique physical effects, like different types of noise and PL.

In this study it was experimented for each sample a different amount of components. The ideal number of components seemed to vary from sample to sample. Often the MCR splits up a pure emission spectra in many non-physical components. Other times it did the latter for some spectra, where at even higher number the analysis did not split signals that could be unique and have different causes. So there are rarely a correct number of components for a analysis but 5-7 components showed to be the most ideal number in the experiments done. The number of components used for the analysis of the different wafers is selected by trial. For the elected number of components, the author has been looking for results with some criteria's. First a result where the spectrum has been divided in to the number of DRL's know from the literature, second where the one DRL is not divided into more components of significantly value, third as few components as possible with noise, at best only where the noise is represented in only one component. As seen in Fig. 3.8 the different DRL's is somewhat separated. BB is component 1, but has also a part that is noise throughout the plot, D3 & D4 is represented as component

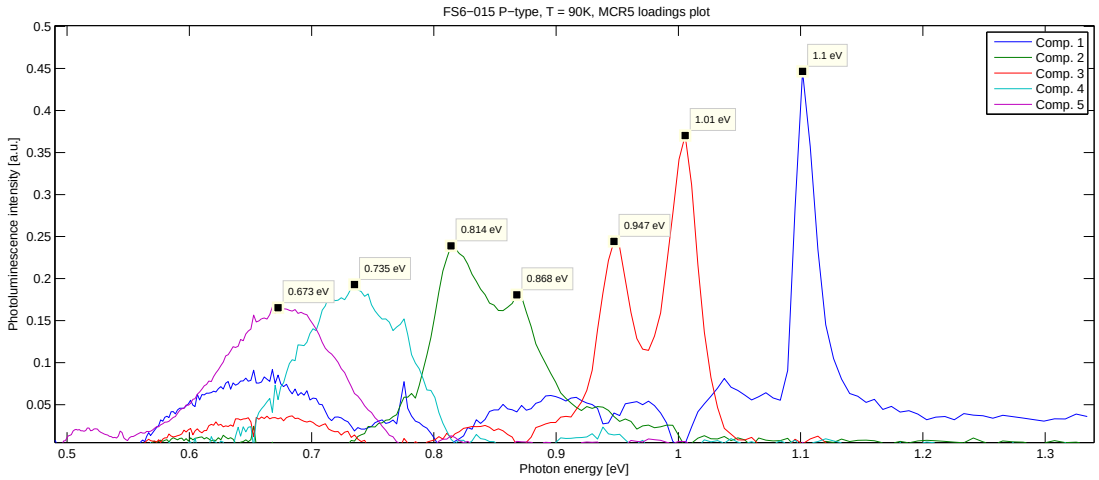

Fig. 3.8: FS6-015-MCR5-plot

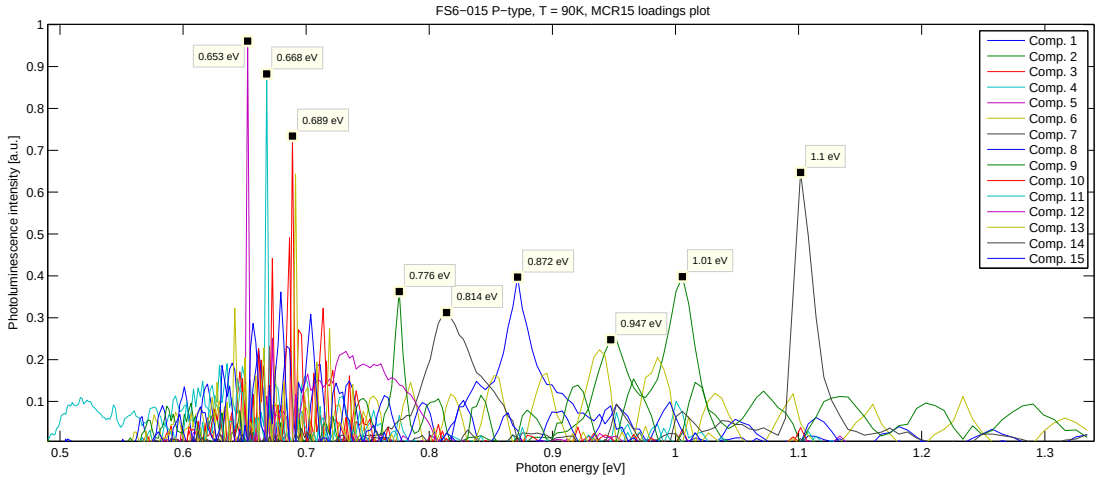

Fig. 3.9: FS6-015-MCR15-plot

3, D2 & D1 is represented as component 2. 0.7 on the other and is separated in two different components (4 & 5). A perfect plot where if D3 & D4 and D2 & D1 where split and the two components of 0.7 merged. Higher number of components were used as seen in Fig. 3.9. Here D3 & D4 is still not separated but D2 & D1 are, unfortunately the high number of components for this wafer divides the 0.7 EV signal into many components and the noise is also divided into several components. For this wafer (FS6-015) the author concluded that five components is the best way to present the recording. In addition to study the MCR spectral plots, the PL-images for each component has been studied in order to take the decision on the number of components to be used. For the different components, the PL-images have been examined for if they only contain noise, or if different components are more or less similar and other effects. For every wafer the mentioned method of dividing the number of components has been implemented.

There are several strengths with using MCR analysis versus only selecting an interval of bands to produce PL-images. First, each PL-image can easily be represented as a plot of its spectrum, this gives us information of what energies that has produced the particular image. Second, with some effort and trials, the MCR's noise can be completely removed showing clearer and more

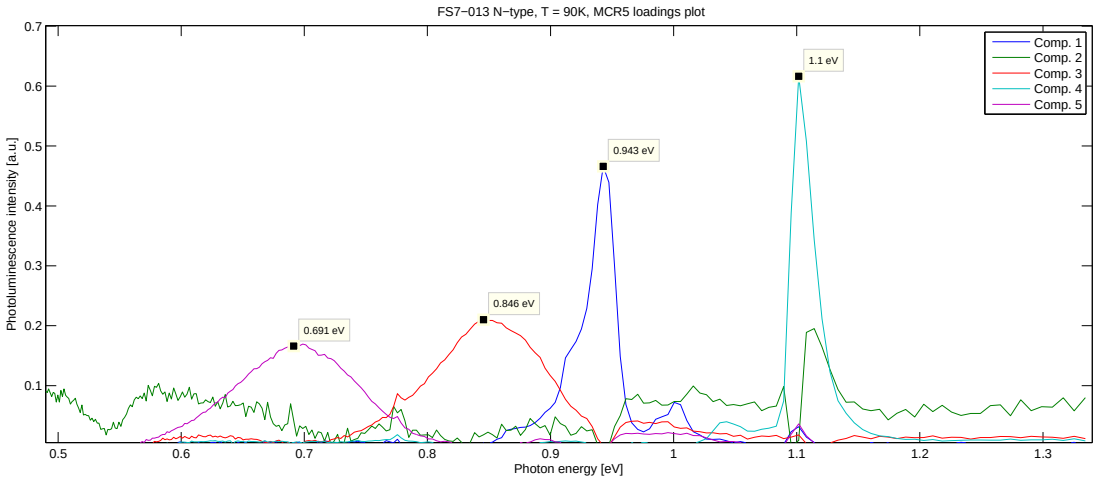

(a) FS7-013, MCR5-plot

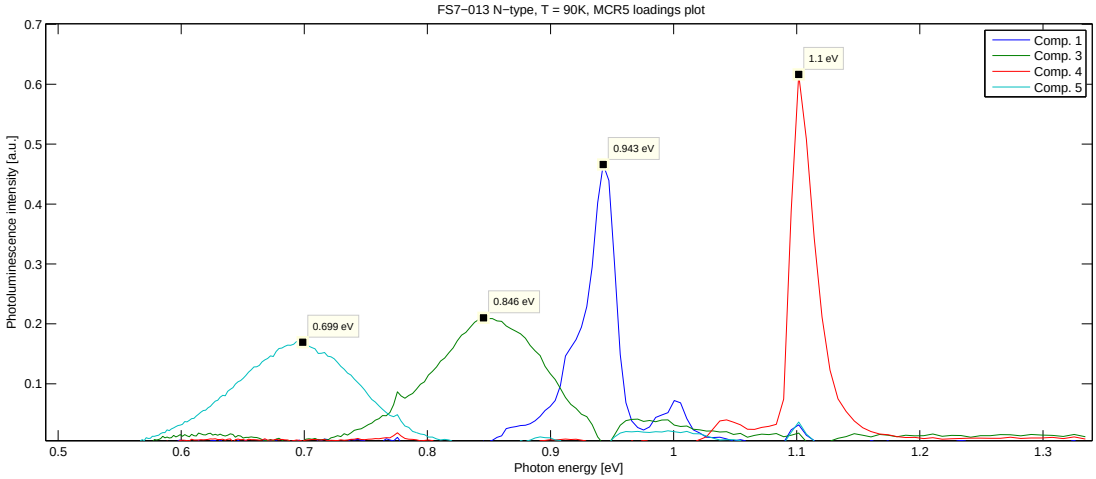

(b) FS7-013, MCR5-plot. Where the noise component is removed

Fig. 3.10: Shows a MCR5-plot of FS7-013, where in (a) all components is included, but at (b) the noise component is removed.

correct PL-images, as shown in Fig. 3.10. Thirdly and last as shown in Fig. 3.11 the PLS Toolbox, used for the MCR analysis yields an elegant way to show separate components in one PL-image.

3.5.3 Photoshop

Photoshop from Adobe Systems Inc., was used as an efficient way to compare the PL images for different components or band-interval with the EBSD images. The software is also used to create some of the figures.

For the comparison between EBSD and hyperspectral images a manual procedure was developed on how to present and compare the images. First the RGB picture of wafer, taken before the EBSD analysis was edited to enhance the contrast in the picture in order to see the grain

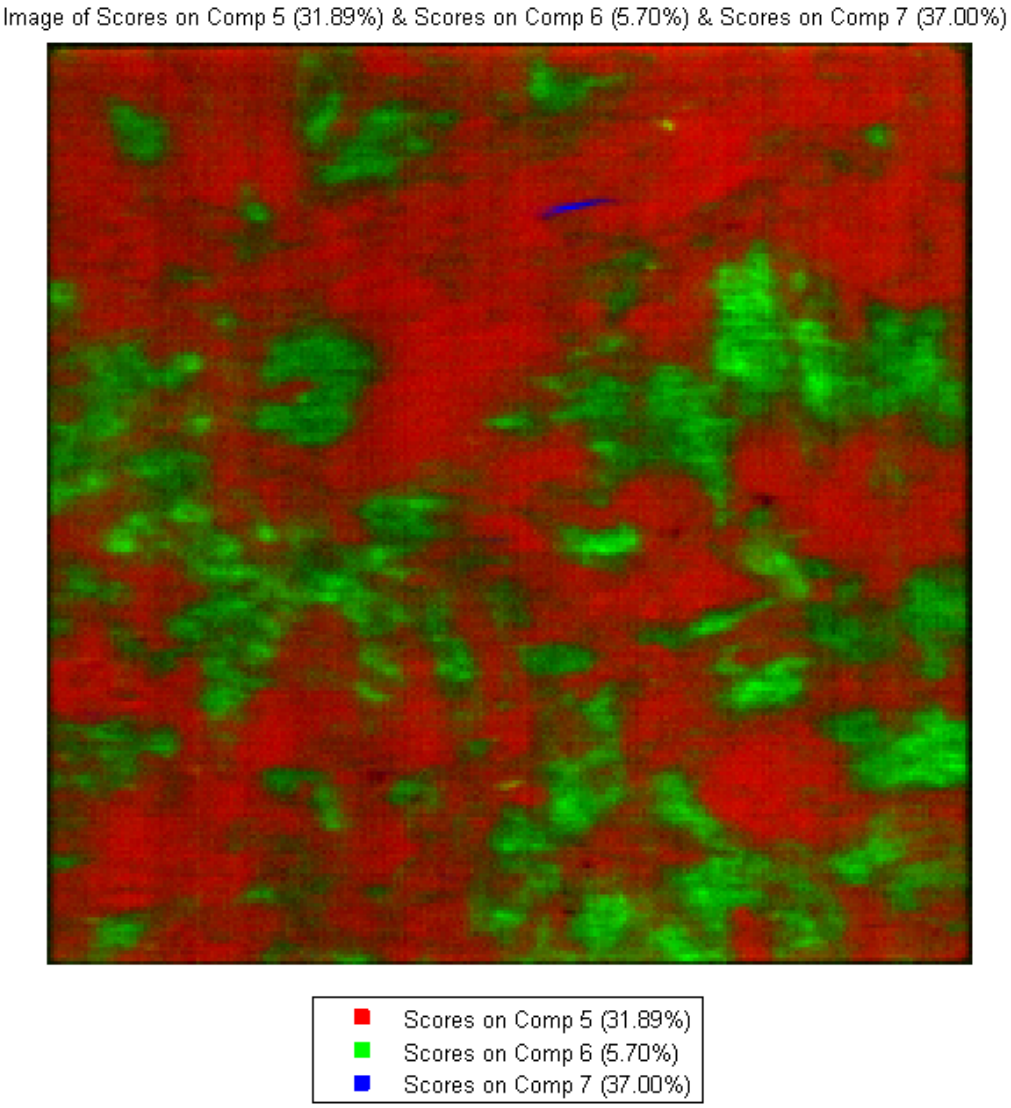

Fig. 3.11: For the MCR7-analysis for FS8-015, three of the components (5, 6 & 7) is added in the same image, seperated by colors as shown in the figure.

boundaries better. Then the EBSD picture was placed in the picture as a separate layer and carefully placed to be sure it is above the exact place where the recording was done. Then the layer is copied and placed to the left of the area as seen in Fig. 3.12 (a). Then a mask in the RGB picture is made covering this exact area of the wafer and all the PL-images is added to the picture as separate layers. Now the images to each component of the MCR analysis or the selected spectra can be compared with the EBSD scan to the left, an example is seen in Fig. 3.12 (b). To study in detail where exact on the EBSD image the illuminated areas on the hyperspectral images are, the EBSD imaged placed as a layer on top of the hyperspectral images was made visible and invisible, again and again. This can unfortunately not be demonstrated in a paper.

(a) EBSD imaged placed on wafer

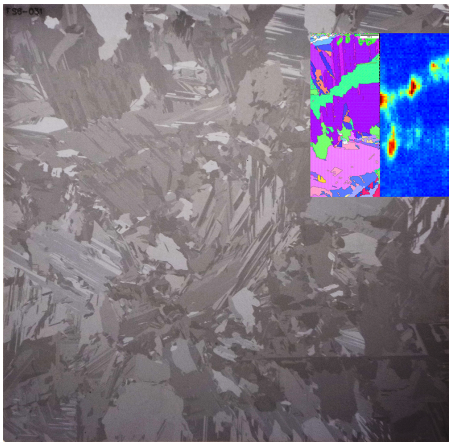

(b) EBSD and hyperspectral imaged placed on wafer

Fig. 3.12: (a) Shows the EBSD imaged scaled to the right relative dimensions and placed left to the area it represents. (b) Shows the EBSD imaged scaled to the right relative dimensions and placed left to a hyperspectral image for the same area.

3.5.4 OIM Analysis

OIM Analysis is the software where EBSD pictures could be produced from recorded data in the OIM Data Collection Application. The application could also edit the pictures through dilution and other noise-removing features and visualize the data in several ways. The pictures produced was exported as TIFF-files. The procedure used with the recordings in this thesis was to rotate the image -87 degrees around the ND/A3-axis. Then a grain CI standardization were performed with grain tolerance angle at 5 and minimum grain size at 2, this increased the average CI. To remove noise from the images grain dilation with grain tolerance and minimum grain size on 5 was used on a copy of the original.

Chapter 4

Results & Discussion

4.1 Hyperspectral Images

Earlier studies with the use of hyperspectral imaging has proven to be technology well suited for characterization of multicrystalline solar cells [25]. Earlier studies have also shown MCR analysis to be an effective method to distinguish different emission signals out from a PL-image conducted on wafers cooled down to low temperatures [10]. In this section findings from the hyperspectral images are presented. These are related to differences in P- and N-type, regarding the appearance of the red zone and differences in DRL for the D3 and D4 energy band, together with different intensity levels for BB.

4.1.1 Differences in red zone for P- and N-type

Red zone appears during the solidification process of Si ingots. The Red zone denotes the outer parts of a silicon ingot that are alongside the crucible and at the top surface. In Fig. 4.1 it is worth noting the intensity bar on the right side. For the N-type the BB is relatively intense compared to the P-type wafers. The reference wafer, has no visible circle indicating the presence of PL. This is expected due to the fact that no Fe contamination were added. However, the interesting difference is the apparent inversion of where (a) and (b) have the most intense PL-signal.

High purity crucibles and purified silicon nitride are used for the production of the wafers in this study. These wafers contained iron levels 60 and 20 times, less than what is common for standard crucibles and silicon nitride, respectively. It was also found that this enhanced the control of iron contaminations from the surroundings [24]. That being said, Kvande et al. also reported that the interstitial iron concentration in the P-type reference wafer is higher at the bottom due to segregation. Thus, most of the iron impurities of the samples are due to the added iron-contamination and not due to interstitial iron. Therefore, the total iron contamination in the wafers cut from the bottom of the ingot should be higher than the bulk.

(a), (c) and (d) shown in Fig. 4.1 are all from the lower part of the ingot. They are either the 13th or 15th wafer cut from the ingot, where the numbering starts from the bottom. The N-type wafer (e) (cut much higher up in the bulk), has no particular sign of any circles due to red-zone for band-to-band PL. For the P-type wafer (b), cut only a little higher, the red zone appears to be slightly less present. In the BB image of FS6-031 as shown in Fig. 4.2 (a) a noticeable large area where FS6-015 have signal, appears to be absent. However as seen in (b) in the same figure, the PL signal from 0.7 have high intensity and broad distribution in the same area where the BB-signal differs between FS6-015 and FS6-031. A weakness is the low PL intensities for both the BB images in the P-type compared to the N-type. This means, if the intensity bars were set to the same levels, the same weak signal in the same areas might appear in the N-type

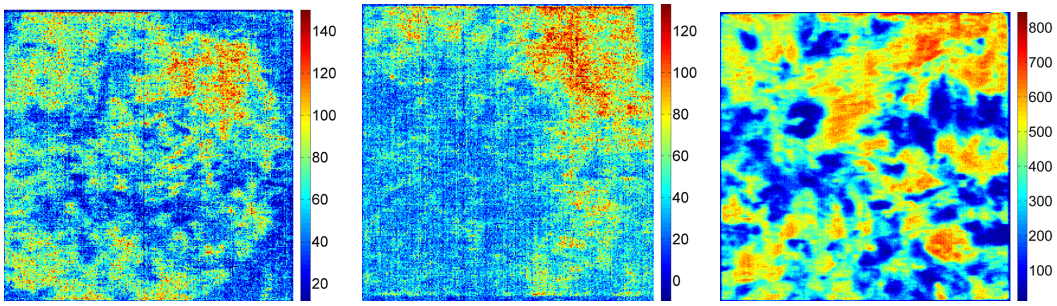

(a) BB found in FS6-015 **(b)** BB found in FS6-031 **(c)** BB found in FS8-015

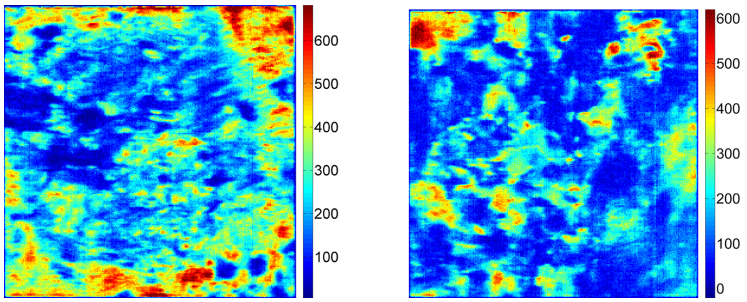

(d) BB found in FS7-013 **(e)** BB found in FS7-162

Fig. 4.1: Comparison of the Band-to-band (BB) found in all the mc-Si wafers used in this study. The upper three are of P-type and the lower two are of N-type. The intensity scales are located on the right hand side.

wafer. This is clearly related to the position from the ingot where the wafer was cut and might be worth further examination by later studies.

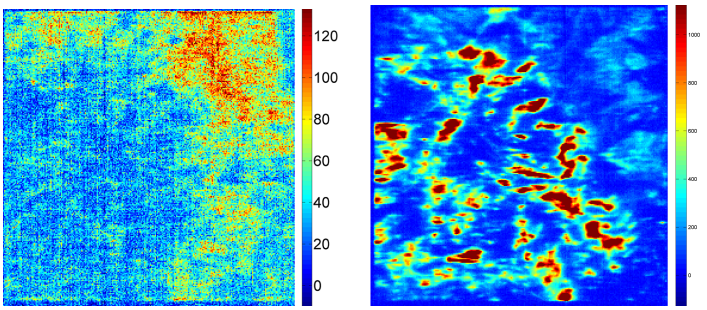

(a) FS6-031 BB **(b)** FS6-015 0.7

Fig. 4.2: Two PL-images of FS6-031 BB & 0.7

4.1.2 Differences in N-type vs P-type

One of the interesting findings in this study is the apparent absence of D3 & D4 in the two N-type wafers. D4 in particular. This has also been seen in an earlier preliminary pilot study performed by Olsen et al. [27], so the chances of this being an error in the recordings is unlikely. The absence of D3 & D4 is very striking in Fig. 4.3, where (a) is a N-type wafer, which only has PL of 0.7, D1-D2, VID3 and BB. For the corresponding PL-images in the area of D3 and

D4 to FS7-013[11], small intense dots are visible which are characteristic for the presence of VID3 [9]. The images from the other wavebands are only weak signals and can most probably be attributed to noise. For the P-type wafer however, seen in Fig. 4.3 (b), both D3 & D4 are present in addition to the DRL-bands found in (a). These mentioned differences for N- and P-type do also to some degree appear in FS6-031 and FS7-162, seen in Fig. 4.4. In (a) the D4 signal is present, but with low intensity. In the corresponding PL-image for D4[12], PL is seen near the edge to the left and right side of the image. In the same plot there is also an apparent presence of either D3 or VID3. In the D3 PL-image as for FS7-013 only small intense dots are visible. Thus, the proof of VID3 and the absence of D3. The implications of these findings are: For the N-type wafers used in this study, there are no or weak PL-signals in the D3-band. However, for the D4-band there are no PL-signals from wafers in the bottom of the ingot, but weak signals do appear higher up.

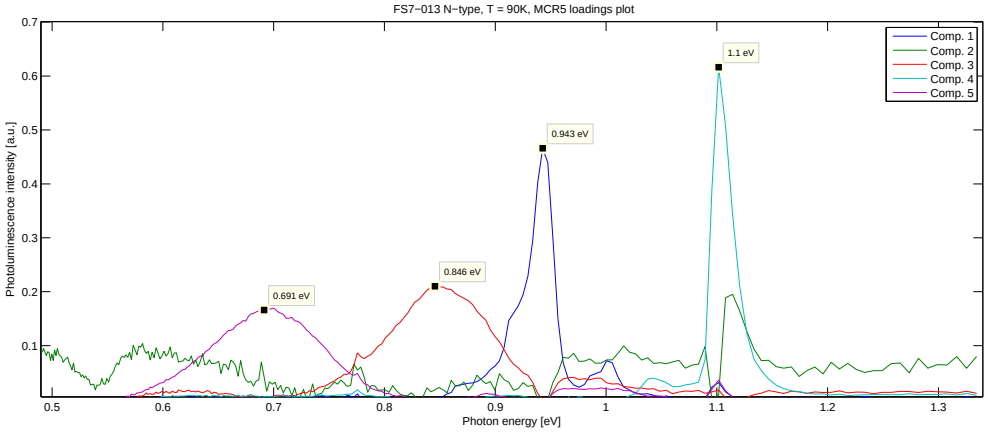

(a) FS7-013, MCR5 Plot

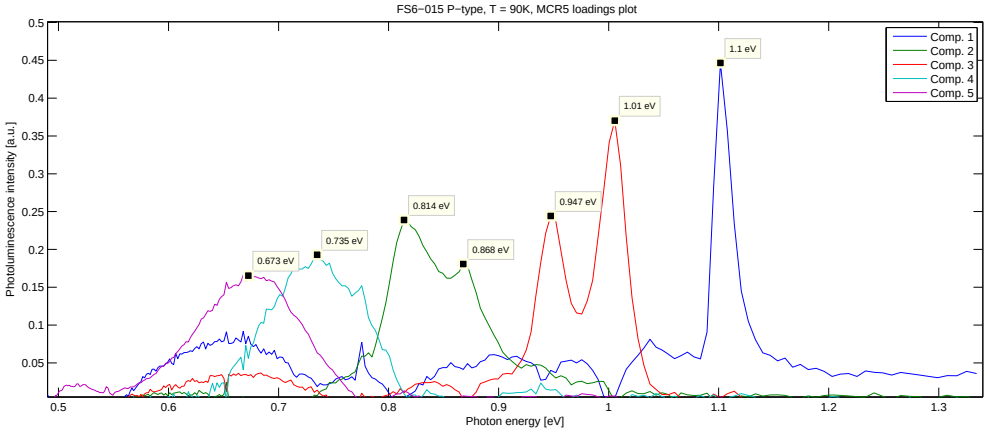

(b) FS6-015, MCR5 Plot

Fig. 4.3: (a) The plot of FS7-013 is from a MCR5 analysis, where D3-D4 is missing. (b) The plot of FS6-015 where D3-D4 are positively present.

The causes to the difference in DRL's of N- and P-type are unclear. It could be related to the different impurities introduced through doping. For P-type, Boron (B) is the dopant. This leads

[11] see Appendix D.1
[12] see Appendix D.2

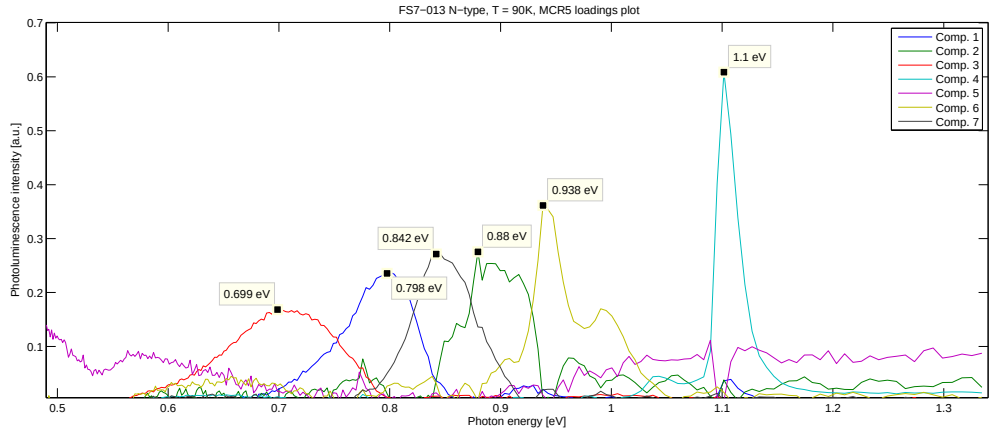

(a) FS7-162, MCR7 Plot

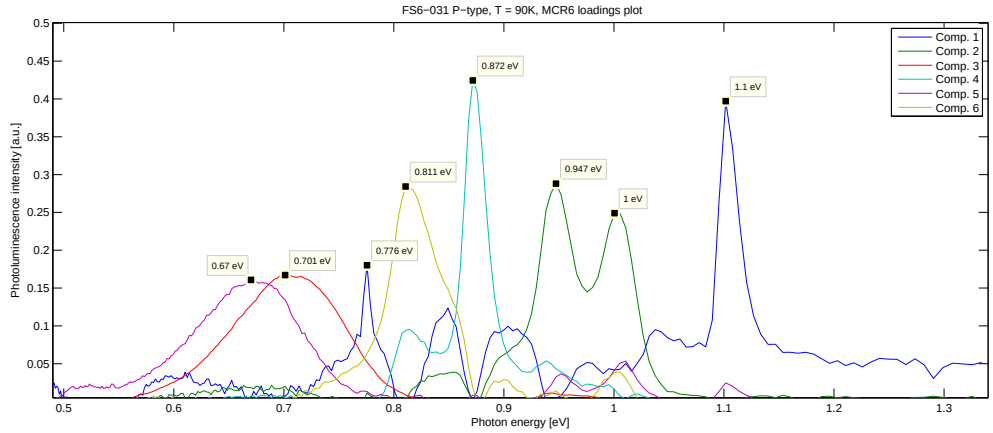

(b) FS6-031, MCR6 Plot

Fig. 4.4: (a) Plot from the MCR7 analysis of FS7-162, where D4 is missing and the probable presence of a weak D3. (b) Plot from the MCR6 analysis of FS6-031 were both D4 and D3 are positively present.

to formation of FeB, which results in reduced carrier lifetimes [30]. For N-type, phosphor (P) is the dopant and have thus no formation of FeB. The N-type, P-type and the reference wafer are made out of the same furnace and the basis for the production of these ingots were high purity crucibles and purified silicon nitride. Which means, the only difference between the produced wafers should be the different doping and how the Fe contaminants react with the doped atoms.

In Figure 4.5 the plot of the reference wafer can be seen. Here both D4 and VID3 are present, with the same argument as for the other wafers earlier mentioned earlier. Thus, no presence of the D3-type DRL. A plausible finding is therefore that the formation of FeB in P-type wafers causes a defect, which generates PL-signals of the D3-type. Furthermore, comparing all the band-to-band PL-images for all the wafers in Fig. 4.1, weak intensities are seen for BB in the Fe-contaminated P-type wafers, but relatively strong intensities in the rest (N-type and reference P-type). The effect is probably caused by the difference in the minority carrier lifetime between N- and P-type and can be explained by SRH recombination from interstitial Fe defects. For the ingot to the P-type Fe contaminated wafers in this study, Kvande et al. have reported unusually strong trapping at crystal defects for as-cut wafers [24]. Further, they showed no trapping phenomenon, not even at the bottom of the P-type reference ingot. Which explains the reduced intensity for BB in the P-type Fe contaminated wafers and suggest a clear relation between

trapping and iron doped in to this ingot. This also coincide with what findings by G. Coletti et al. [5], where the lifetime values in N-type Fe ingots were found to be eight times higher than for P-type Fe ingot, after gettering and hydrogenation on the P-type ingo.

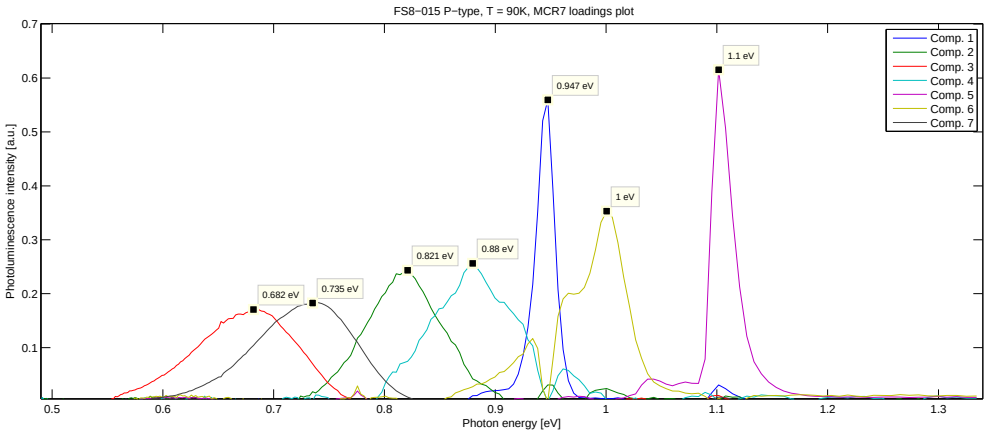

Fig. 4.5: MCR7 plot of the P-type reference wafer FS8-015, where D4 and VID3 are found, however no or weak signals from D3.

4.1.3 Macro Images

The idea of recording images using a macro lens was to get a higher resolution of the area where the EBSD images later were to be recorded. Very late in this master thesis, it was discovered that the PL-images had been rotated 90 degrees to the right compared to the wafers (if seen with the number written on the top). The wafers when scanned should in this case have been placed 90 degrees to the left when performing the hyperspectral recordings to avoid the mistake. However, this led to the fact, that the macro images were record at the wrong place of the wafer. Therefore these images are not used in the results of this thesis. Nonetheless, as seen in Figure 4.6 these have a much higher resolution of the hyperspectral images and could have been a valuable complementary contribution to comparison of EBSD scans and hyperspectral images.

The considerable difference in intensity values between (a) and (b) are due to unequal exposure times, thus the intensities can not be compared. The macro recording (a) had a relatively shorter exposure time than the normal recording (b) and is why the emission intensity in (a) appears weaker than for (b). However, the distribution of the photoluminescence intensities are the same. A enhanced script of the noise removal should also be written, since the used script to remove noise in the pictures shown is the same, thus optimize for recordings using the normal objective. From the figure it can be seen that considerable noise is present in (a), but appears also to be more in focus than (b) which seems without noise, thus out of focus. However, the MCR analysis removed parts of the noise in separate components.

4.2 EBSD Scans compared with Hyperspectral images

Comparinson of the EBSD scans and the hyperspectral images recorded, as shown in Fig. 4.7 and 4.8, shows an apparent correlation between these two characterization techniques. The illuminated areas in the PL-images appears to have a similar form and contours as in different

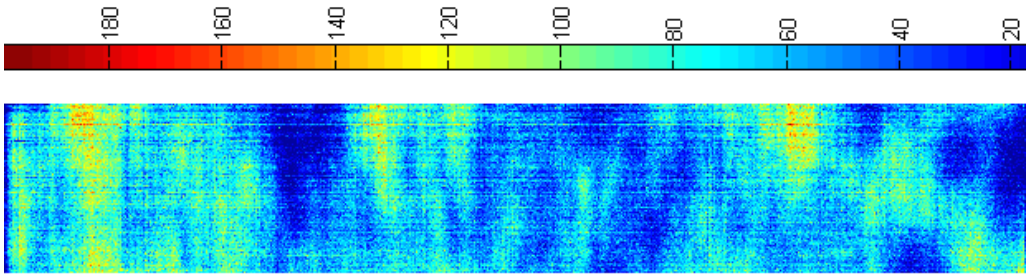

(a) FS7-013 component 4 (BB) MCR5, macro

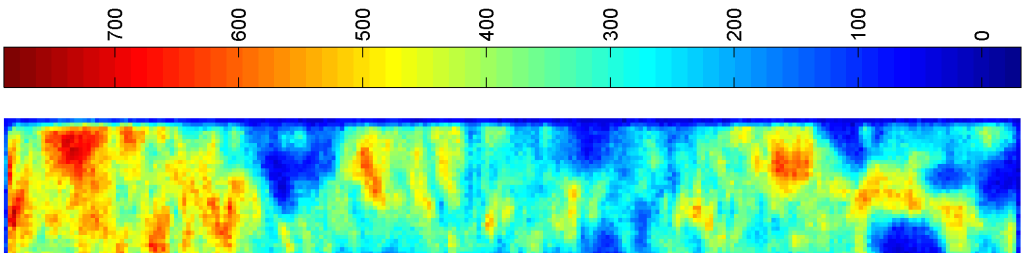

(b) FS7-013 BB

Fig. 4.6: (a) is from a recording carried out with use of the macro lens. Component 4 is for this comparison selected, which where identified as the BB-component from a corresponding MCR-plot. The MCR-analysis was set to calculate five components of FS7-013. (b) is a from a recording carried out with the use of the normal lens. The specified waveband for BB in FS7-013 is selected, and only the same area of the wafer as in (a) is shown.

areas in the EBSD scan with the same crystal orientation[13]. When presented in the mosaic made with Photoshop, as described in Section 3.5.3, it came very clear that shapes and contours in the different scans and recordings seemed to match. In Fig. 4.8 the EBSD scan and PL-images from the MCR-analysis are shown. In Fig. 4.7 the EBSD scan is compared with the PL-images from the DRL-bands and BB. This to show that both using the MCR-analysis and a selection of spectra result in contours which match the contours in the EBSD scan.

The match is more prominent in some of the samples, like for FS6-031 and FS8-015. In FS6-031 the green area matches very well with the PL-image for D2. For FS8-015 emission with energies at 0.7 eV are forming a contour around the big purple area in upper right of the EBSD scan and most of the 0.7 PL-signal comes from some areas where different crystallographic orientations meet. In FS6-015 the correlation is predominantly visible for the second component. However, if we look at three components in one picture as shown in Fig. 4.9, it can be seen that the green area (component 2) of the image to the right matches the turquoise area in the EBSD scan. Further the red areas (component 1) in the upper part of the PL-image seems to correspond to the purple area in the EBSD scan.

Now what does this tell us? It means that these two methods for characterization of silicon materials can be used together to further unveil new knowledge. It should be a topic for further studies to explore these two methods in order to get a better knowledge of the origins of the DRL-lines.

[13]Identified as areas with the same color

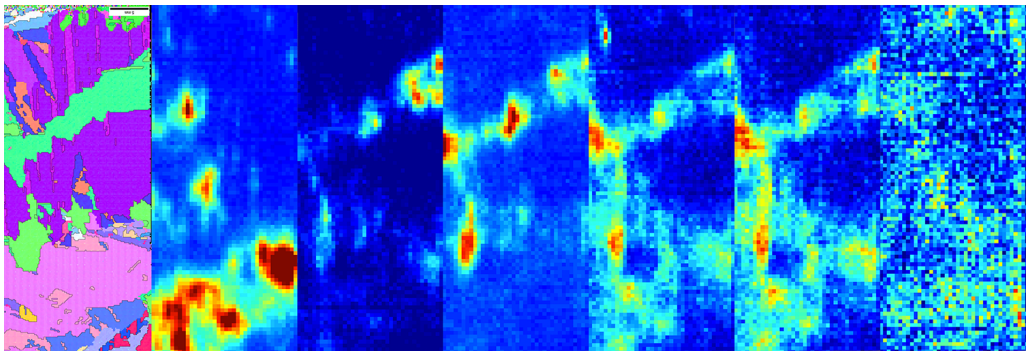

(a) FS6-031 DRL

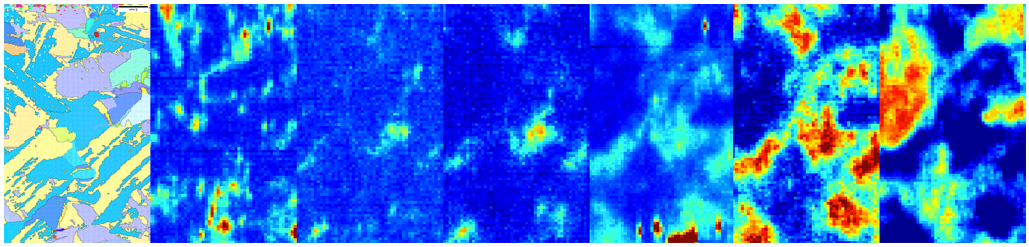

(b) FS8-015 DRL

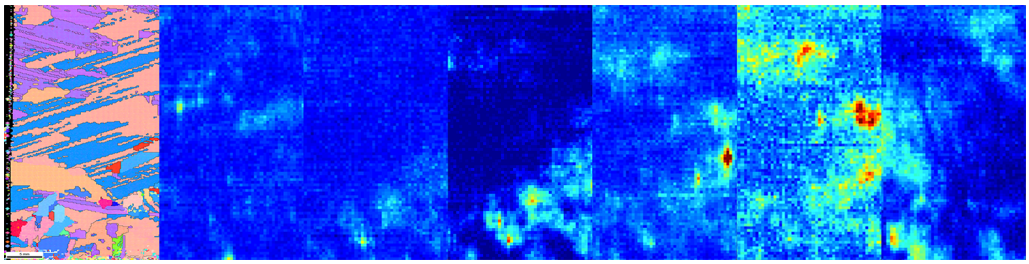

(c) FS7-162 DRL

Fig. 4.7: EBSD recording for the specific wafer compared with its corresponding PL-images from D-bands and spectra from selected points. Within each subfigure the images is arranged from the left as follows; 0.7, D1, D2, D3, D4 and BB.

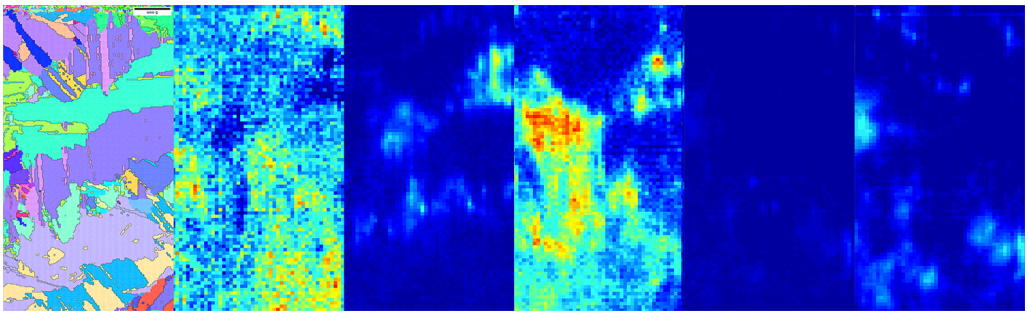

(a) FS6-015 MCR5

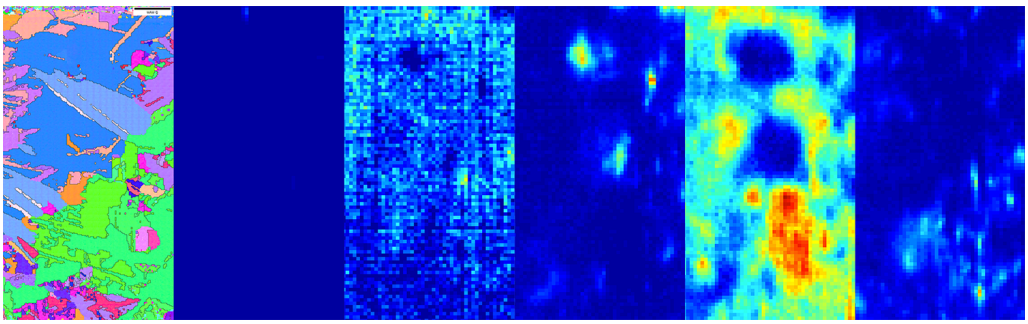

(b) FS7-013 MCR5

Fig. 4.8: EBSD recordings to the left compared with the corresponding PL-images, from the MCR-analysis. The components of the PL-images are arranged, from left, in ascending order (1,2,3 etc.).

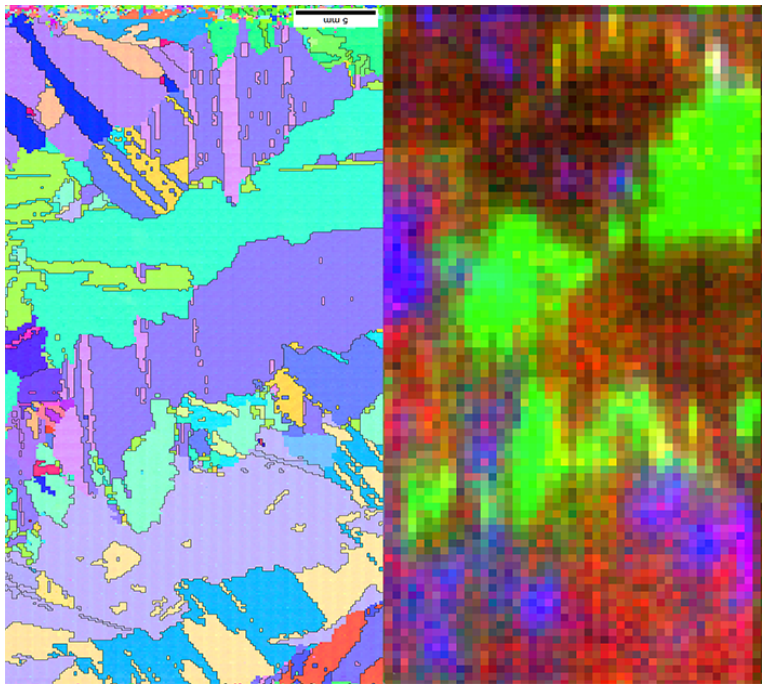

Fig. 4.9: EBSD recordings to the left compared with the corresponding PL-images, from the MCR-analysis. The components 1,2 % 5 are shown in the same image, labeled with different colors. Component 1 is red, component 2 is green and component 5 is blue.

Chapter 5

Conclusion

This continued research on the use of hyperspectral imaging as a characterization method has confirmed the conclusions of earlier studies: It is a qualified, nondestructive and relatively quick method for analyzing DRL caused by radiative recombination of the SRH-type. The results of the MCR-analysis of different wafers varied and did not always generate physical valid spectra. Further, a proper output from a MCR-analysis demands effort and trails to find the right amount of components. However, the effort results in an effective method to distinguish different emission signals and how these differ between separate types of wafers. The use of SEM and EBSD gave detailed images regarding the crystallographic orientations of the samples. The downside of the latter technique is the destructiveness and time-consumed process to perform the analysis.

From the hyperspectral study there are several key findings. The apparent absence of both D3 and D4 at the bottom of the ingot in the N-type wafer. A weak D4-band for a N-type wafer high up in ingot. For both N-type wafers (from the bottom and high up in the ingot), there were an apparent absence or very weak signal for D3, but instead presence of a strong VID3. BB intensities showed to be relatively much weaker for Fe contaminated P-type wafer, than for Fe contaminated N-type or the P-type reference wafer. The use of a macro lens for hyperspectral images showed to generate images with higher resolutions than for a normal. Further the PL distribution is equal for both lenses, as expected.

This study is the first attempt to examine how EBSD scans could correlate with images produced from hyperspectral imaging. The results are promising and have shown an apparent correlation between these to characterization techniques. Different forms and contours present in both the EBSD scan and the corresponding hyperspectral image were found. A broad signal with peak around 0.7 eV in the reference P-type wafer seems to correlate with where different crystallographic orientations meet. For a Fe contaminated P-type wafer one crystallographic direction appeared to match the PL-image for D2.

5.1 Further research

A weakness in this study is the limited number of wafers studied. E.g. there were no P-type wafers from high up in the ingot as one of the N-type were. The N-type reference wafer used were a monocrystalline wafer, later studies should have a mc-Si N-type reference wafer. It would be interesting to preform a comparison between a range N- and P-type wafers distributed from the bottom to the top of the ingot. That could falsify or support the findings about differences in D3 and D4 for N-type and P-type, if it is just a particular case or a characteristic for Fe contaminated as-cut wafers, produced in the same way.

Another study is to undergo an analysis of if the BB emissions are generally intense in the red zone at bottom of the ingot or just an odd case.

The use of macro objectives, generates a much higher resolution for the hyperspectral images. Therefor, to achieve a more detailed comparison on what type of correlation that are to be found between EBSD scans and hyperspectral images, macro or other high resolution objectives would be an advantage for the further studies. The downside are big file sizes and much slower MCR-analysis.

At last an extended study based on this work to look at the correlation between images from EBSD scan and hyperspectral imaging, is something that can be very interesting to see what correlations which will be found. But much of preliminary studies between crystallographic structure and correlation with PL-images can be performed with the use of good RGB images of the wafer and hyperspectral images, as explained in this thesis just without the EBSD scan. Then interesting areas are easier to identify before more through studies with the use of EBSD.

Bibliography

[1] T. Arguirov. *Electro-optical properties of dislocations in silicon and their possible application for light emitters.* PhD thesis, der Brandenburgischen Technischen Universität Cottbus, Cottbus, Germany, 2007.

[2] L. Arnberg, M. Di Sabatino, and E. J. Øvrelid. Solidification of silicon for electronic and solar applications. *JOM*, 63(10):38–42, October 2011.

[3] T. G. Brown and D. G. Hall. Optical emission at 1.32 μm from sulfur-doped crystalline silicon. *Applied Physics Letters*, 49(5):245–247, August 1986.

[4] C. J. Chen. *Physics of Solar Energy.* John Wiley & Sons, Inc., Hoboken, New Jersey, 2011.

[5] G. Coletti, R. Kvande, V. D. Mihailetchi, L. J. Geerligs, L. Arnberg, and E. J. Øvrelid. Effect of iron in silicon feedstock on p- and n-type multicrystalline silicon solar cells. *Journal of Applied Physics*, 104(10):104913, 2008.

[6] A. de Juan, R. Tauler, R. Dyson, C. Marcolli, M. Rault, and M. Maeder. Spectroscopic imaging and chemometrics: a powerful combination for global and local sample analysis. *TrAC Trends in Analytical Chemistry*, 23(1):70–79, January 2004.

[7] M. Di Sabatino and G. Stokkan. Defect generation, advanced crystallization, and characterization methods for high-quality solar-cell silicon. *Physica Status Solidi Applied Research*, 210(4):641–648, October 2012.

[8] N. A. Drozdov, A. A. Patrin, and V. D. Tkachev. Recombination radiation on dislocations in silicon. *Pis'ma Zh. Eksp. Teor. Fiz.*, (11):651–653, June 1976.

[9] A. S. Fløe. *Hyperspectral Imaging as a Tool for characterization of Mulitcrystalline Silicon Wafers.* PhD thesis, Norwegian University of Life Sciences, Ås, Norway, 2014.

[10] A. K. Fremme. Hyperspectral photoluminescence scans of mc- si wafers analysed through multivariate curve resolution (mcr). Master's thesis, Norwegian University of Life Sciences, 2014.

[11] P. Friedlingstein, S. Solomon, G.-K. Plattner, R. Knutti, P. Ciais, and M. R. Raupach. Long-term climate implications of twenty-first century options for carbon dioxide emission mitigation. *Nature Climate Change*, 1(9):457–461, November 2011.

[12] T. H. Gfroerer. Photoluminescence in analysis of surfaces and interfaces. *Encyclopedia of Analytical Chemistry*, 36(1):9209–9231, September 2000.

[13] M. Grätzel. Dye-sensitized solar cells. *Journal of Photochemistry and Photobiology C: Photochemistry Reviews*, 4(2):145–153, October 2003.

[14] M. Grätzel. Mesoscopic solar cells for electricity and hydrogen production from sunlight. *Chemistry Letters*, 34(1):8–13, 2005.

[15] M. A. Green. *Solar Cells: Operating Principles, Technology and System Applications*. University of New South Wales, Kensington, 1998.

[16] D. M. Haaland, J. A. Timlin, M. B. Sinclair, M. H. Van Benthem, M. J. Martinez, A. D. Aragon, and M. Werner-Washburne. Multivariate curve resolution for hyperspectral image analysis: applications to microarray technology. In R. M. Levenson, G. H. Bearman, and A. Mahadevan-Jansen, editors, *Spectral Imaging: Instrumentation, Applications, and Analysis II*, volume 4959, pages 55–66. Society of Photo-Optical Instrumentation Engineers Conference Series, July 2003.

[17] P. C. Hemmer. *Faste stoffers fysikk*. Tapir forlag, Trondheim, 1987.

[18] V. Higgs, M. Goulding, A. Brinklow, and P. Kightley. Characterization of epitaxial and oxidation-induced stacking faults in silicon: The influence of transition-metal contamination. *Applied Physics Letters*, 60(11):1369, March 1992.

[19] J. Hjelen. *Scanning elektron-mikroskopi*. Norges Tekniske Høgskole, 1986.

[20] D. Hull and D. J. Bacon. *Introduction to dislocations*. Butterworth-Heinemann, Oxford, 5th edition, 2011.

[21] J.W. Morris, Jr. Materials science - chapter 4: Defects in crystals p.76-107. Notes from the course MSE205 given at UC Berkeley.

[22] C. Kittel. *Introduction to solid state physics*. John Wiley & Sons, Inc., Hoboken, NJ, 8th edition, 2005.

[23] C. Krause, D. Mankovics, H.-M. Krause, T. Arguirov, and M. Kittler. On the origin of intense luminescence at 0.93 eV from multi-crystalline silicon. *Journal of Applied Physics*, 114(3):034902, July 2013.

[24] R. Kvande, L. J. Geerligs, G. Coletti, L. Arnberg, M. Di Sabatino, E. J. Øvrelid, and C. C. Swanson. Distribution of iron in multicrystalline silicon ingots. *Journal of Applied Physics*, 104(6):064905, Februrary 2008.

[25] T. Mehl. Karakterisering av multikrystallinske solceller ved bruk av hyperspektral avbildning. Master's thesis, Norwegian University of Life Sciences, 2014. Now PhD student, part of the Hyperspectral research group at NMBU.

[26] T. Mehl. Defect related photoluminescence in solar cells studied by spectral imaging. Presented in a poster at CSSC-8 (8th International workshop on crystalline Silicon for Solar Cells), May 2015.

[27] E. Olsen, I. Burud, and A. S. Flø. Unpublished studies of hyperspectral imaging of inter band gap radiative recombination - results from wafers produced by ntnu and contaminated with impurities. May 2014.

[28] S. Ostapenko, I. Tarasov, J. P. Kalejs, C. Haessler, and E.-U. Reisner. Defect monitoring using scanning photoluminescence spectroscopy in multicrystalline silicon wafers. *Semiconductor Science and Technology*, 15(8):840–848, June 2000.

[29] S. Ranjan, S. Balaji, R. A. Panella, and B. E. Ydstie. Silicon solar cell production. *Computers & Chemical Engineering*, 35(8):1439–1453, August 2011.

[30] S. Rein. *Lifetime Spectroscopy: A Method of Defect Characterization in Silicon for Photovoltaic Applications*. Springer, Berlin New York, 2005.

[31] J. W. Rohlf. *MODERN PHYSICS from α to Z^0*. John Wiley & Sons, Inc., New York, 1st edition, 1994.

[32] R. Sauer, J. Weber, J. Stolz, E. R. Weber, K.-H. Küsters, and H. Alexander. Dislocation-related photoluminescence in silicon. *Applied Physics A*, 36(1):1–13, January 1985.

[33] T. Sekiguchi and K. Sumino. Cathodoluminescence study on dislocations in silicon. *Journal of Applied Physics*, 79(6):3253, December 1996.

[34] M. Tajima, Y. Iwata, F. Okayama, H. Toyota, H. Onodera, and T. Sekiguchi. Deep-level photoluminescence due to dislocations and oxygen precipitates in multicrystalline si. *Journal of Applied Physics*, 111(11):113523, 2012.

[35] J. S. Townsend. *Quantum Physics: A Fundamental Approach to Modern Physics*. University Science Books, Sausalito, California, 2010.

[36] P. Würfel. *Physics of Solar Cells: From Basic Principles to Advanced Concepts*. WILEY-VCH, Weinheim, 2 edition, 2009.

[37] G. M. Wyller. Master thesis in preparation. Norwegian University of Life Sciences, May 2015.

Appendices

A Laser intensity

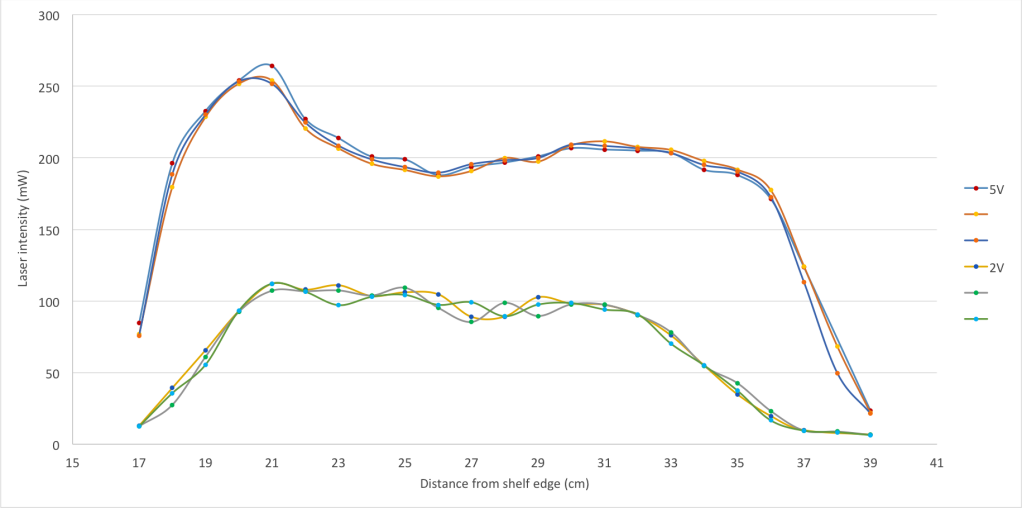

Fig. A.1: The figure shows the intensities from the laser beam for two different voltages. The y-axis shows the intensity in mW and the x-axis is the distance from the shelf edge.

A.2

B EBSD Images

B.1 FS6-015B, Fe, P-type

Summary:

FS6-015B
Operator: sem
Calibration: 0.528900 0.568000 0.779200
Working Distance: 30.000000

Number of points: 55360
Number of good points: 55310

Dimensions:
X Min: 0.00 microns
X Max: 23850.00 microns
Y Min: 0.00 microns
Y Max: 51750.00 microns
Step: 150.00 microns

Average Confidence Index: 0.82
Average Image Quality: 59.19
Average Fit [degrees]: 1.09

Phases: Silicon

Rotate: Manual (RD 0.0∞, TD 0.0∞, ND -87.0∞)
Cleanup - Grain CI Standardization (tolerance 5.0, min size 5, Multi Row 1)

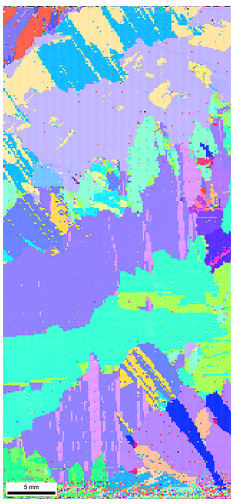

(a) Original EBSD-map (IPF - Inverse pole figure)

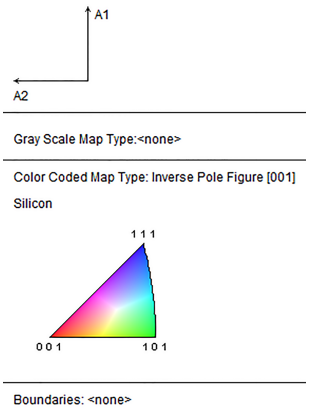

(b) Crystallographic orientation map

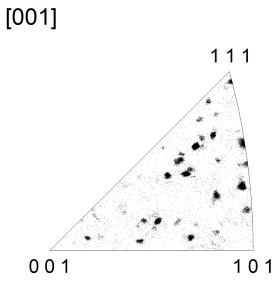

(c) Distribution of the Crystallographic orientation

Fig. B.2

B.2 FS6-031B, Fe, P-type

Summary:

fs6-031B

Operator: sem
Calibration: 0.432092 0.535219 0.750422
Working Distance: 30.000000

Number of points: 38184
Number of good points: 37692

Dimensions:
X Min: 0.00 microns
X Max: 19200.00 microns
Y Min: 0.00 microns
Y Max: 44250.00 microns
Step: 150.00 microns

Average Confidence Index: 0.76
Average Image Quality: 66.50
Average Fit [degrees]: 1.33

Phases: Silicon

Rotate: Manual (RD 0.0∞, TD 0.0∞, ND -87.0∞)
Cleanup - Grain CI Standardization (tolerance 5.0, min size 2, Multi Row 0)

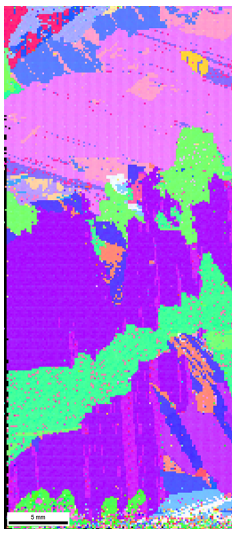

(a) Original EBSD-map (IPF)

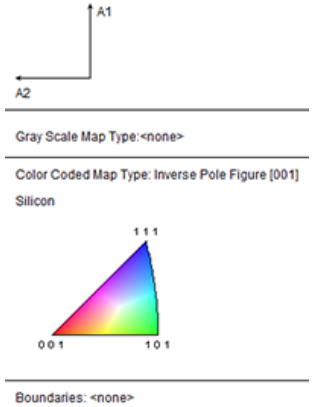

(b) Crystallographic orientation map

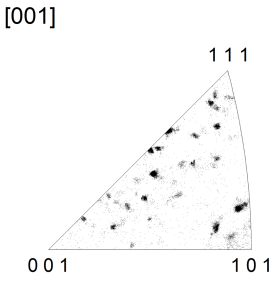

(c) Distribution of the Crystallographic orientation

Fig. B.3

B.3 FS7-013B, Fe, N-type

Summary:

FS7-013B

Operator: sem
Calibration: 0.454168 0.482957 0.791479
Working Distance: 30.000000

Number of points: 55360
Number of good points: 55354

Dimensions:
X Min: 0.00 microns
X Max: 23850.00 microns
Y Min: 0.00 microns
Y Max: 51750.00 microns
Step: 150.00 microns

Average Confidence Index: 0.78
Average Image Quality: 56.37
Average Fit [degrees]: 1.30

Phases: Silicon

Rotate: Manual (RD 0.0∞, TD 0.0∞, ND -87.0∞)
Cleanup - Grain CI Standardization (tolerance 5.0, min size 2, Multi Row 1)

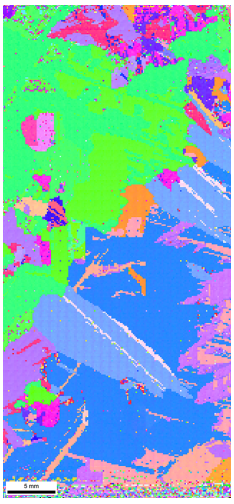

(a) Original EBSD-map (IPF)

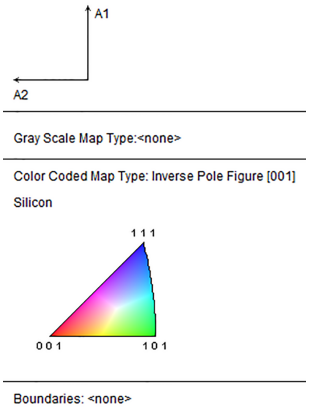

(b) Crystallographic orientation map

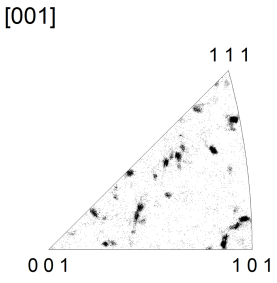

(c) Distribution of the Crystallographic orientation

Fig. B.4

B.4 FS7-162B, Fe, N-type

Summary:

FS7-162B

Operator: sem
Calibration: 0.440000 0.580000 0.760900
Working Distance: 30.000000

Number of points: 50172
Number of good points: 47447

Dimensions:
X Min: 0.00 microns
X Max: 22050.00 microns
Y Min: 0.00 microns
Y Max: 50700.00 microns
Step: 150.00 microns

Average Confidence Index: 0.77
Average Image Quality: 55.75
Average Fit [degrees]: 1.38

Phases: Silicon

Rotate: Manual (RD 0.0∞, TD 0.0∞, ND -87.0∞)
Cleanup - Grain CI Standardization (tolerance 5.0, min size 2, Multi Row 1)

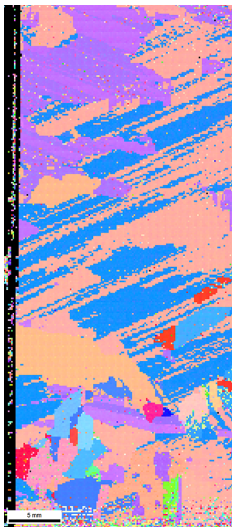

(a) Original EBSD-map (IPF)

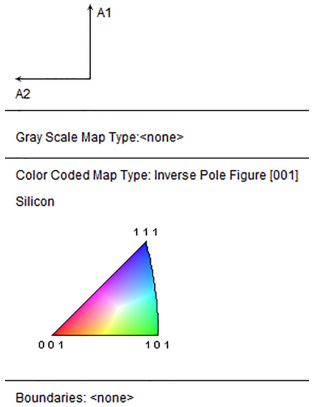

(b) Crystallographic orientation map

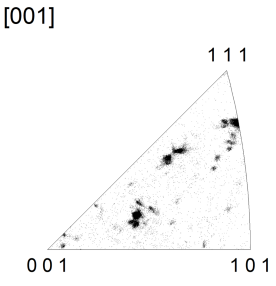

(c) Distribution of the Crystallographic orientation

Fig. B.5

B.5 FS8-015B, reference wafer, P-type

Summary:

FS8-015B

Operator: sem
Calibration: 0.510000 0.490000 0.790900
Working Distance: 30.000000

Number of points: 48597
Number of good points: 48585

Dimensions:
X Min: 0.00 microns
X Max: 24900.00 microns
Y Min: 0.00 microns
Y Max: 43500.00 microns
Step: 150.00 microns

Average Confidence Index: 0.74
Average Image Quality: 60.64
Average Fit [degrees]: 1.17

Phases: Silicon

Rotate: Manual (RD 0.0∞, TD 0.0∞, ND -87.0∞)
Cleanup - Grain CI Standardization (tolerance 5.0, min size 2, Multi Row 0)

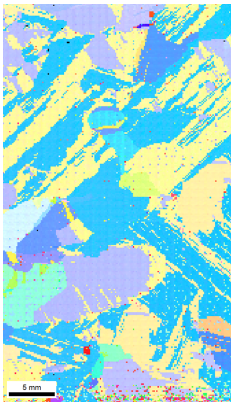

(a) Original EBSD-map (IPF)

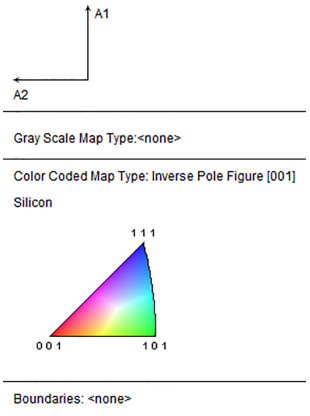

(b) Crystallographic orientation map

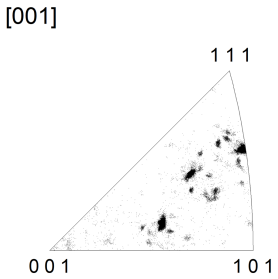

(c) Distribution of the Crystallographic orientation

Fig. B.6

C Matlab code

```
%-------------------------------------------------------------------------
%       Workingscript.m
%-------------------------------------------------------------------------

% #### Renaming ####
fn1 = 'Norsun-mono-N-type-Ref-5V-1';
fn2 = 'Norsun-mono-N-type-Ref-5V-2';
fn3 = 'Norsun-mono-N-type-Ref-5V-3';

% ##### Noise removal #######
% load and subtract calibrate the picture for systematic error-effects
% caused by the camera and removes background noise in the images.
tic
img1 = load_subtract_correctTMfast(fn1);
img2 = load_subtract_correctTMfast(fn2);
img3 = load_subtract_correctTMfast(fn3);
toc

% ##### PL-images on selected recorded bands ######
% This section is used to look at the PL-images for different bands of the
% camera. E.g 32 equals BB. This part is also used to find the positions of
% the edges of the wafer in the image. "img1" was changed to "img2" and
% "img3" to also see for the other two recordings.
imtool(img1(:,:,32),[],'Colormap',jet)
imtool(img1(:,:,49),[],'Colormap',jet)
imtool(img1(:,:,62),[],'Colormap',jet)
imtool(img1(:,:,107),[],'Colormap',jet)
imtool(img1(:,:,141),[],'Colormap',jet)

%######## Ploting before median picture is produced ######
%Used to produce a figure with a spectrum for each of the three
%recordings of the same wafer. This allows an inspection that the spectrum
%are more or less equal
hold on
sp = squeeze(sum(sum(img1,1))); %sum x,y for each z
sp = sp - min(sp); %adjust noise and zero level
plot(sp);

sp = squeeze(sum(sum(img2,1))); %sum x,y for each z
sp = sp - min(sp); %adjust noise and zero level
plot(sp, 'g');

sp = squeeze(sum(sum(img3,1))); %sum x,y for each z
sp = sp - min(sp); %adjust noise and zero level
plot(sp, 'm');
hold off

% ##### Cropping ######
%In this section the positions of the wafer is set
x1 = 70; y1 = 28;
x2 = 317; y2 = 214;
% Now it is again checked if these positions are correct and if there are
% still area that needs to be removed.
imtool(img1((y1):(y2),(x1):(x2),32),[],'Colormap',jet)
imtool(img2((y1):(y2),(x1):(x2),32),[],'Colormap',jet)
imtool(img3((y1):(y2),(x1):(x2),32),[],'Colormap',jet)
% Each image is then cropped
img1C = img1(y1:y2, x1:x2, :);
img2C = img2((y1):(y2), x1:x2,:);
img3C = img3((y1):(y2), x1:x2,:);

% #### Making a Median of the three images ####
tic
```

```
imgMC = MakeMedianImg(img1C, img2C, img3C);
toc

% Again we can check how the median image turned out on different bands
imtool(imgMC(:,:,32),[],'Colormap',jet)
imtool(imgMC(:,:,63),[],'Colormap',jet)
imtool(imgMC(:,:,86),[],'Colormap',jet)
imtool(imgMC(:,:,107),[],'Colormap',jet)

% ##### Export as a MAT file #####
FS6pFe5V015 = imgMC;
tic
save('FS6p015Lys.mat','FS6p015Lys','-v7.3');
toc
% If wanted a new spectrum can be plotted of the median image, to compare
% it with the three other spectra earlier produced.
hold on
sp = squeeze(sum(sum(FS6pFe5V015,1))); %sum x,y for each z
sp = sp - min(sp); %adjust noise and zero level
plot(sp, 'r');
hold off
```

```
%--------------------------------------------------------------------------
%       Dlines.m
%--------------------------------------------------------------------------
%  Script used to produce images for specific selected wavelengths,
%  generating images for BB, D4, D3, D2, D1 and 0.7 eV.

load('Energi_specimOct2014.mat') % loads a matrix with the energy values
% to each band in the camera
load('FS7n5V162'); % loads the hyperspectral image recorded, wanted to
% print figures for the selected spectra

imgMAT = FS7n5V162;


d = 2;
BB=(31-d:31+d);
D1=(98-d:98+d);
D2=(80-d:80+d);
D3=(63-d:63+d);
D4=(51-d:51+d);
D07=(134-d:134+d);

TypeBB=BB;
TypeD4=D4;
TypeD3=D3;
TypeD2=D2;
TypeD1=D1;
Type07=D07;

TypeBBimg= sum(imgMAT(:,:,TypeBB),3);
imtool(TypeBBimg,[],'Colormap',jet)
TypeD4img= sum(imgMAT(:,:,TypeD4),3);
imtool(TypeD4img,[],'Colormap',jet)
TypeD3img= sum(imgMAT(:,:,TypeD3),3);
imtool(TypeD3img,[],'Colormap',jet)
TypeD2img= sum(imgMAT(:,:,TypeD2),3);
imtool(TypeD2img,[],'Colormap',jet)
TypeD1img= sum(imgMAT(:,:,TypeD1),3);
imtool(TypeD1img,[],'Colormap',jet)
Type07img= sum(imgMAT(:,:,Type07),3);
imtool(Type07img,[],'Colormap',jet)
```

```
%-------------------------------------------------------------------------
%   PlotMCRloads.m
%-------------------------------------------------------------------------

load('Energi_specimOct2014.mat');
mcrloads = FS7n162MCR7.loads{2};
figure;
% The line under was used to get proper pdf-prints for the plots
figure1 = figure('Renderer','painters','PaperType','<custom>',...
    'PaperSize',[31.3 13.8],...
    'InvertHardcopy','off',...
    'Color',[1 1 1]);
%To plot only some of the components, then use the line under and uncomment
%the next line.
a= [1 2 3 4 6 7];% 5 6 7  9  11 12 13 ];%13 14 15 16 19 20];
%plot(Ev,mcrloads(:,a))
plot(Ev,mcrloads(:,:)) %Plots all the components and correlates
%the bands where the values are stored to the eV-value, as a result it
%flips the graph.
axis([0.49 1.34 0.005 0.701]); % defines the limits for the axes on the plot

% Defining the name on the axes, title and legend
xlabel('Photon energy [eV]')
ylabel('Photoluminescence intensity [a.u.]')
title(' FS7-013 N-type, T = 90K, MCR5 loadings plot')
legend('Comp. 1','Comp. 2','Comp. 3','Comp. 4','Comp. 5','Comp. 6','Comp. ...
    7','Comp. 8','Comp. 9','Comp. 10','Comp. 11','Comp. 12','Comp. 13','Comp. ...
    14','Comp. 15',...
    'Location','NorthEast')
```

D PL Images for N-type Wafers

D.1 FS7-013, Fe

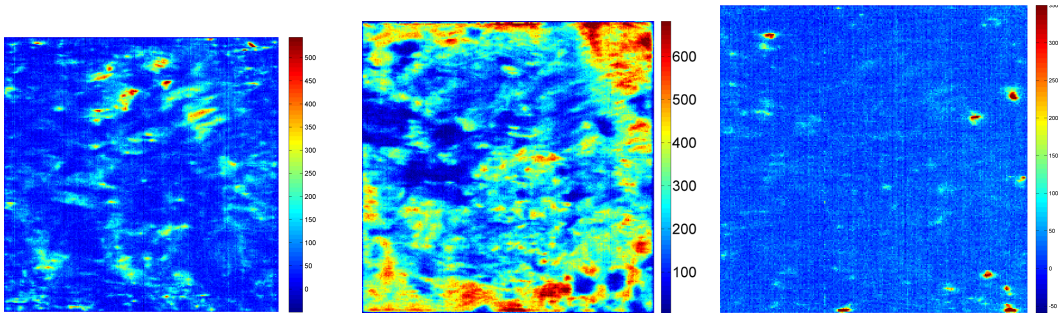

(a) 0.7 (b) BB (c) D1

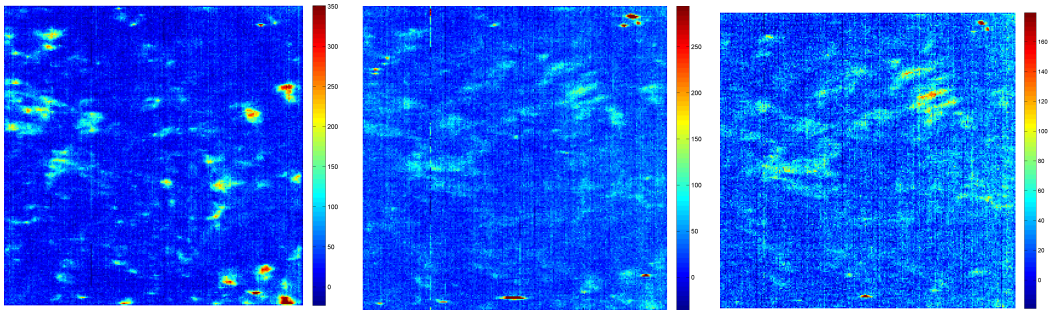

(d) D2 (e) D3 (f) D4

Fig. D.7

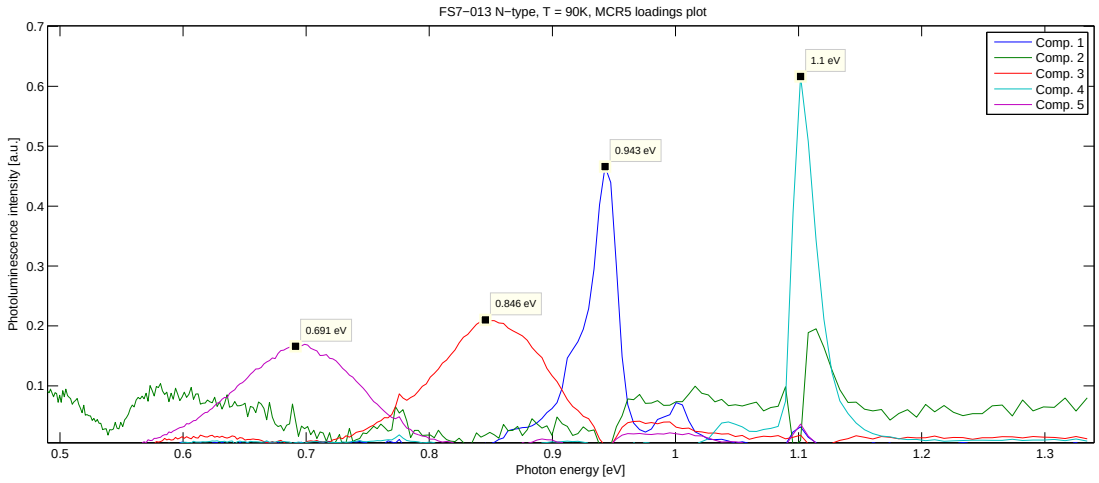

Fig. D.9

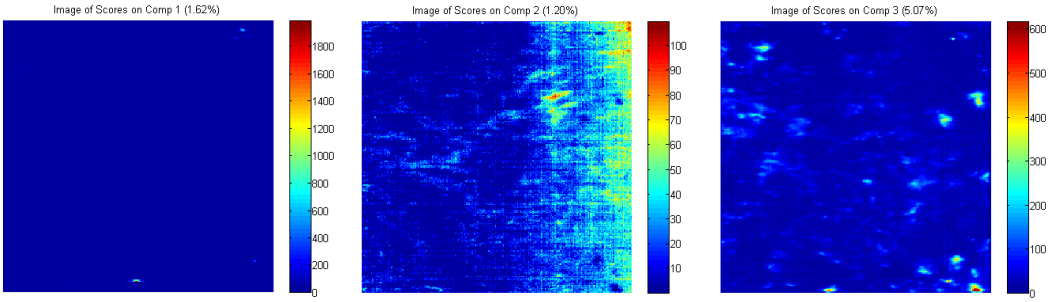

(a) Comp. 1 **(b)** Comp. 2 **(c)** Comp. 3

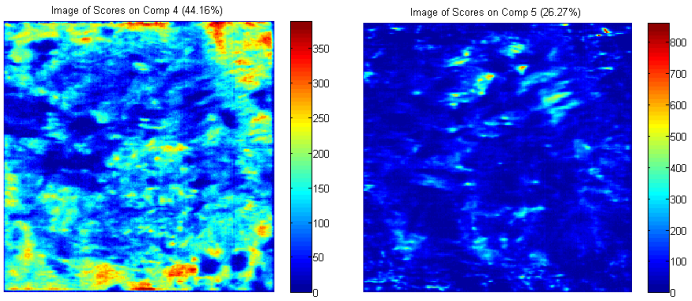

(d) Comp. 4 **(e)** Comp. 5

Fig. D.8

D.2 FS7-162, Fe

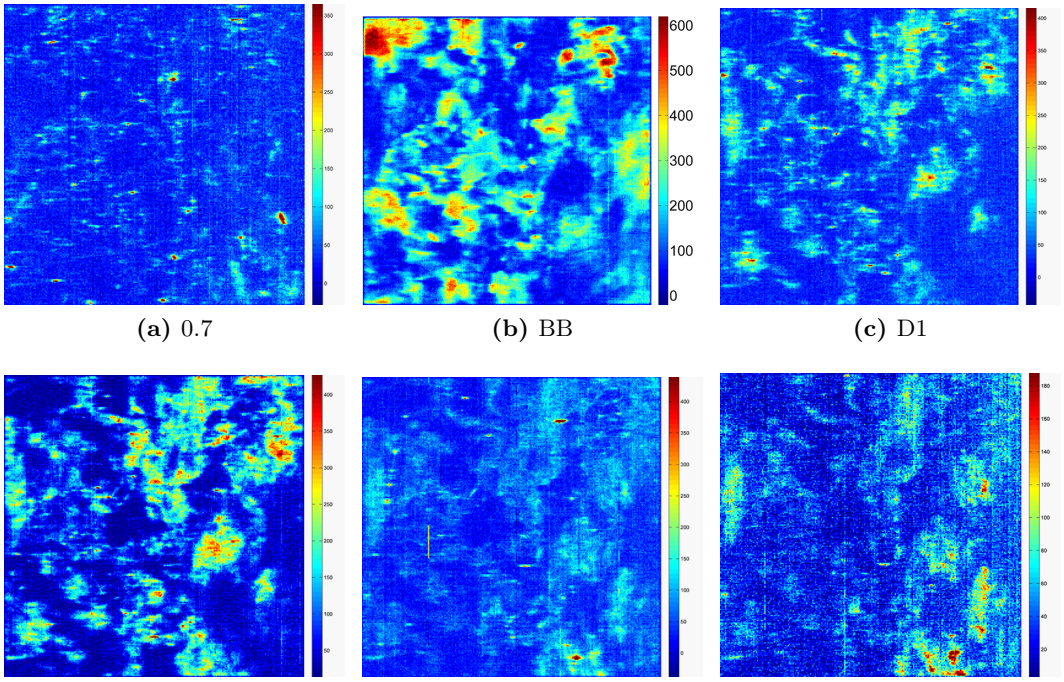

(a) 0.7 **(b)** BB **(c)** D1

(d) D2 **(e)** D3 **(f)** D4

Fig. D.10

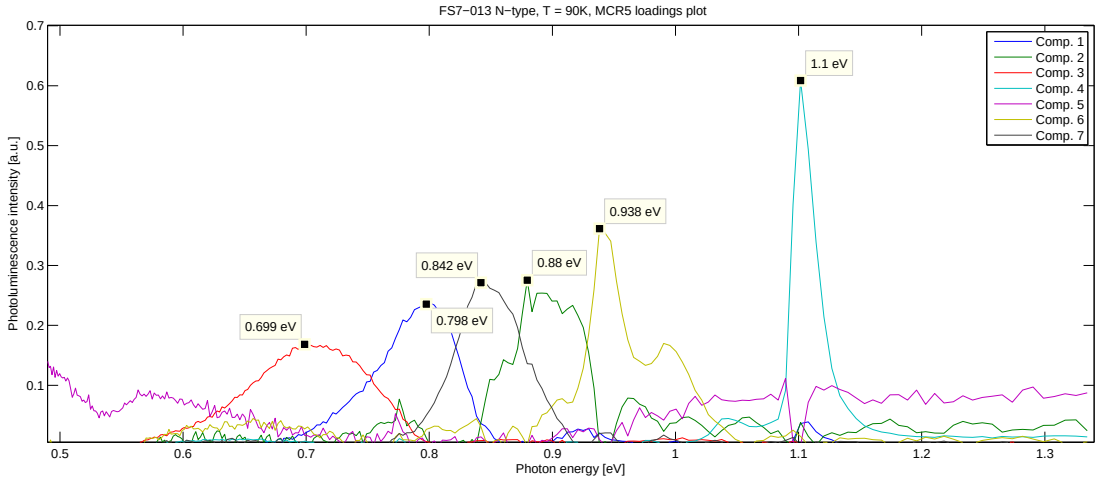

Fig. D.12

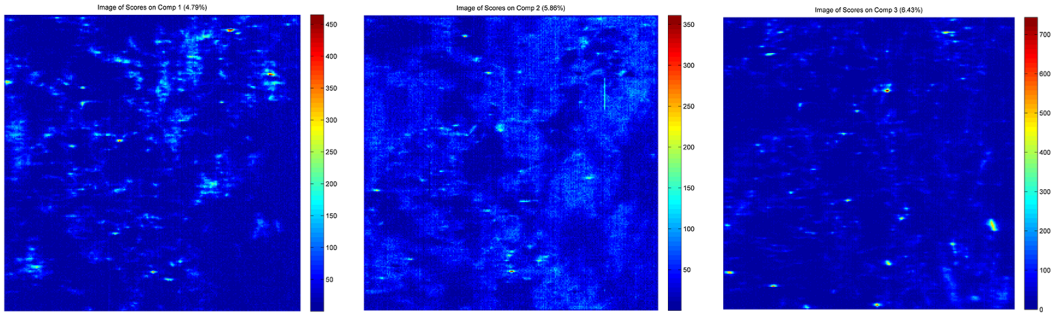

(a) Comp. 1 **(b)** Comp. 2 **(c)** Comp. 3

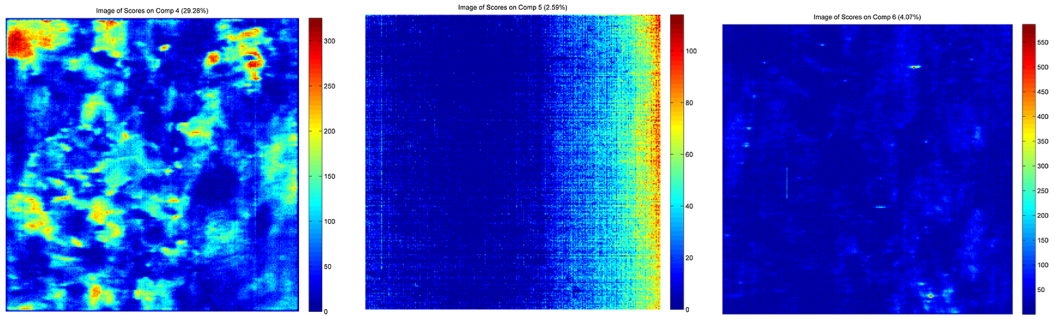

(d) Comp. 4 **(e)** Comp. 5 **(f)** Comp. 6

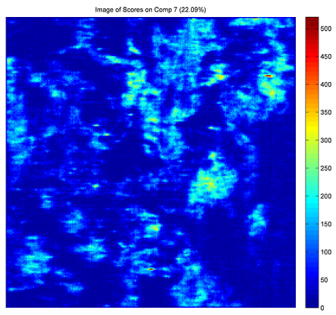

(g) Comp. 7

Fig. D.11

D.3 Norsun, Reference wafer

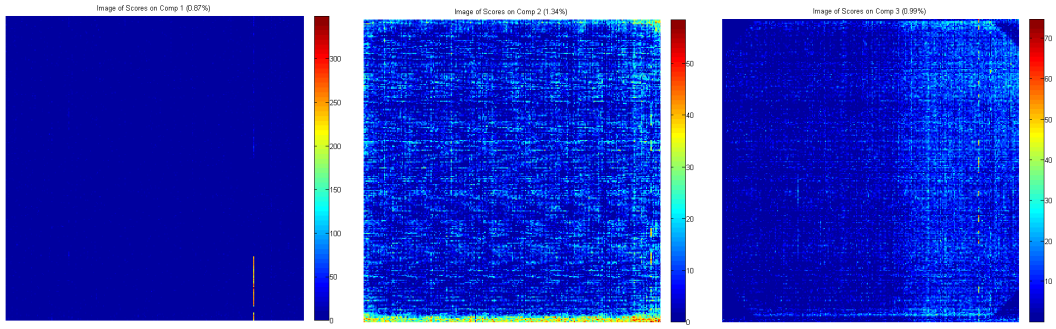

(a) Comp. 1 **(b)** Comp. 2 **(c)** Comp. 3

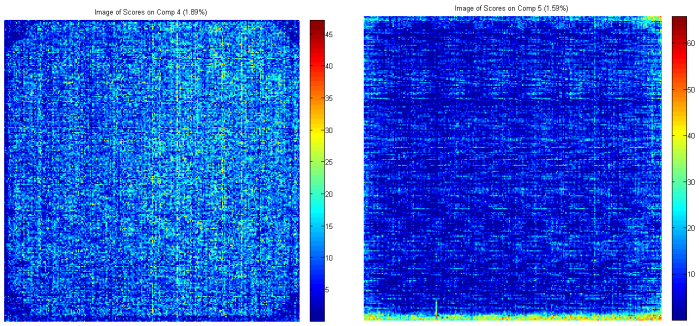

(d) Comp. 4 **(e)** Comp. 5

Fig. D.13

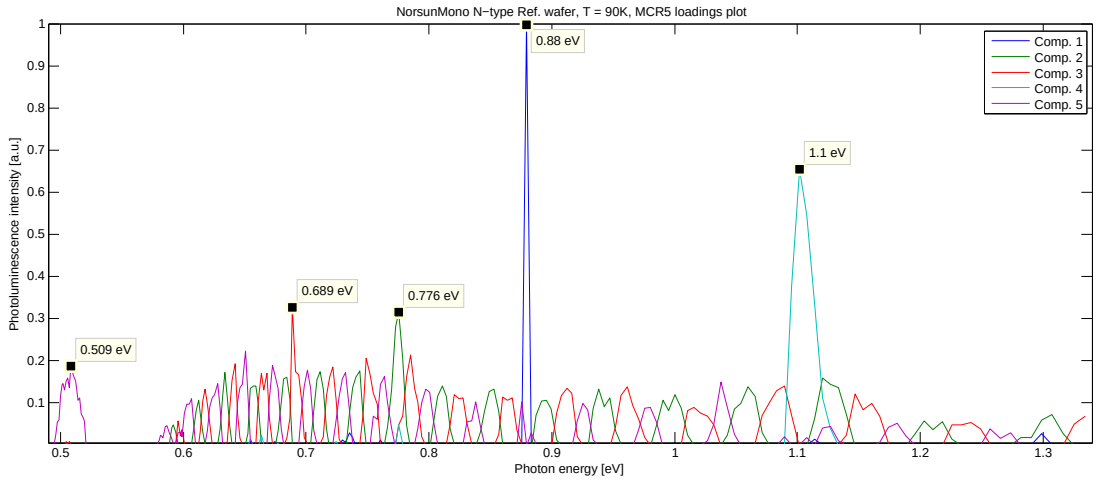

Fig. D.14

E PL Images for P-type Wafers

E.1 FS6-015, Fe

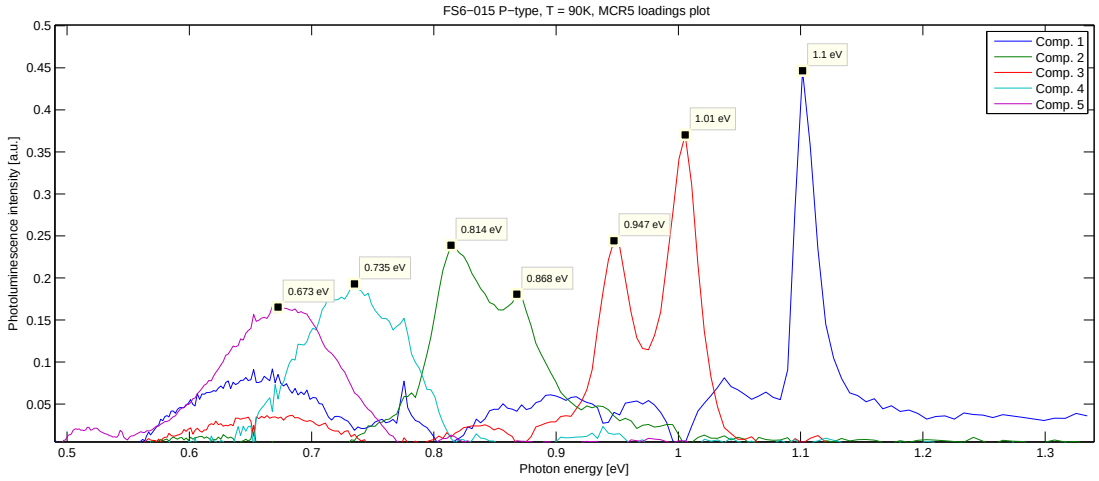

Fig. E.15

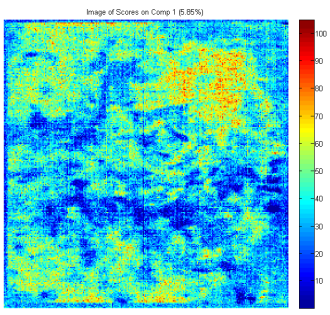

(a) Comp. 1

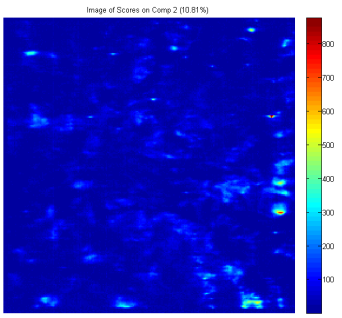

(b) Comp. 2

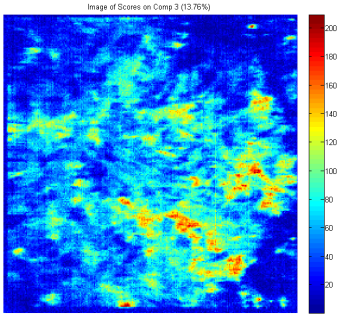

(c) Comp. 3

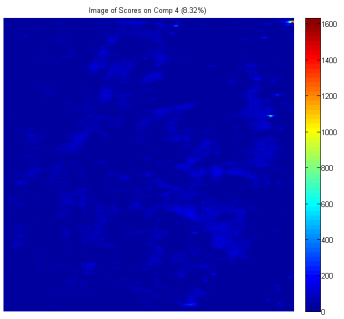

(d) Comp. 4

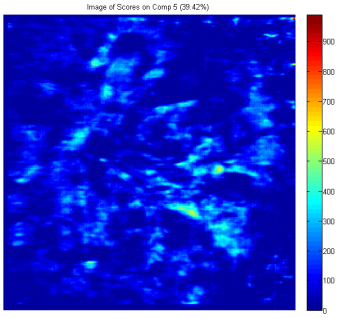

(e) Comp. 5

Fig. E.16

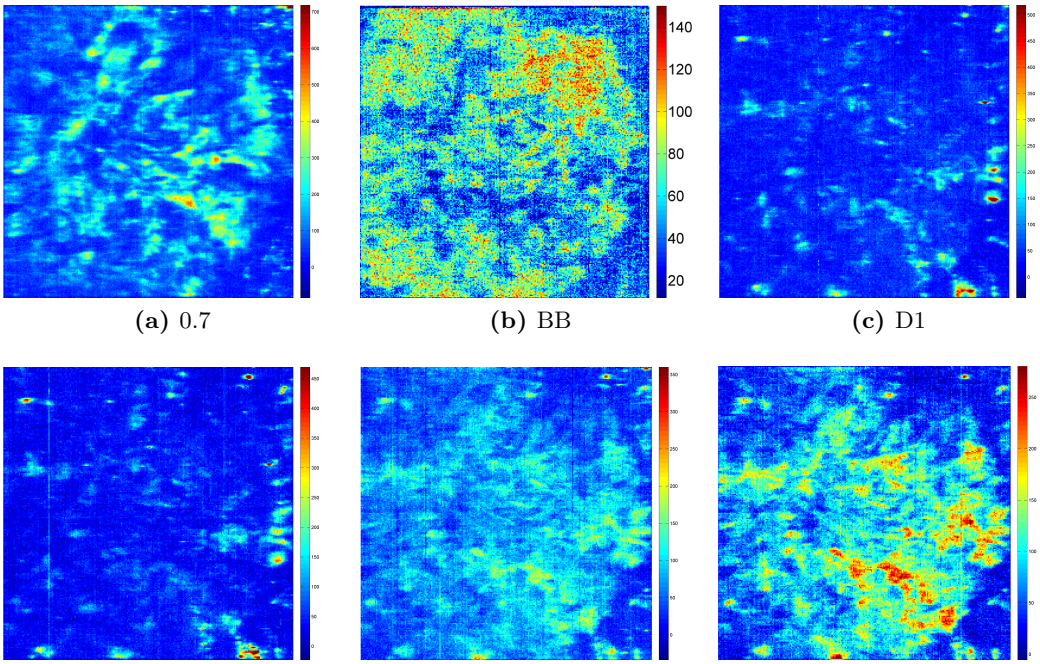

(a) 0.7 **(b)** BB **(c)** D1

(d) D2 **(e)** D3 **(f)** D4

Fig. E.17

E.2 FS6-031, Fe

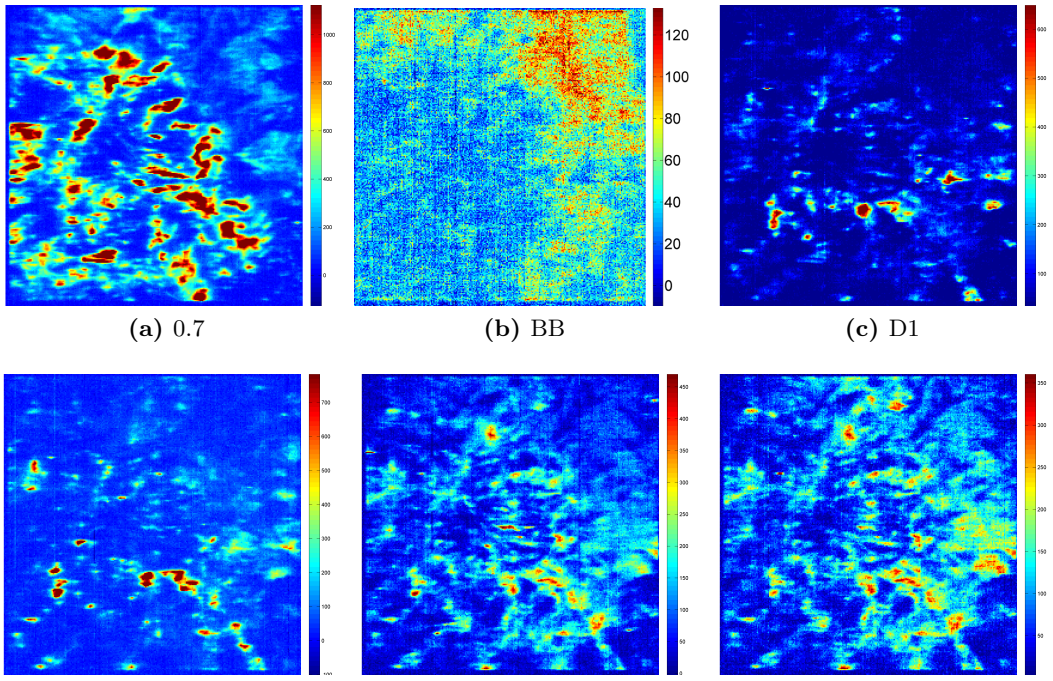

(a) 0.7 **(b)** BB **(c)** D1

(d) D2 **(e)** D3 **(f)** D4

Fig. E.18

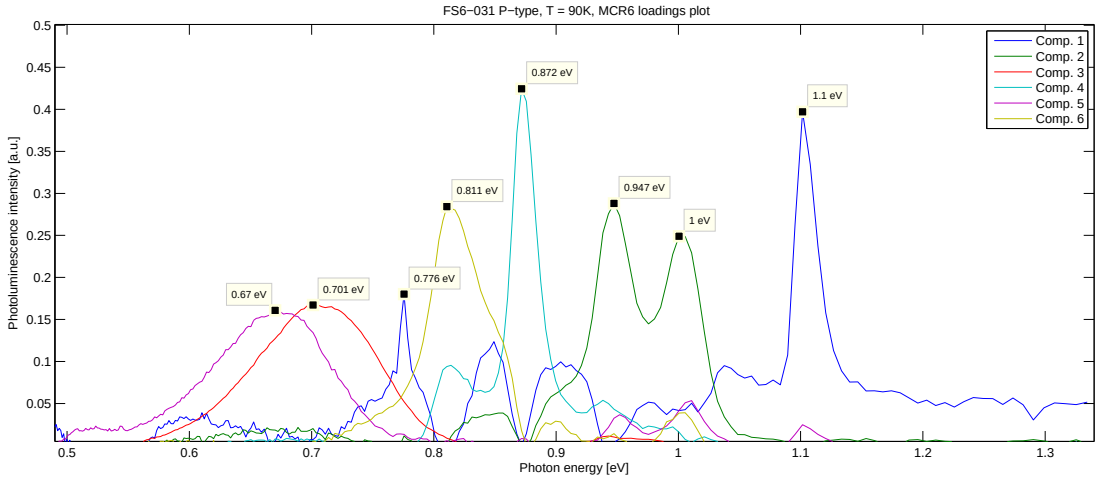

Fig. E.20

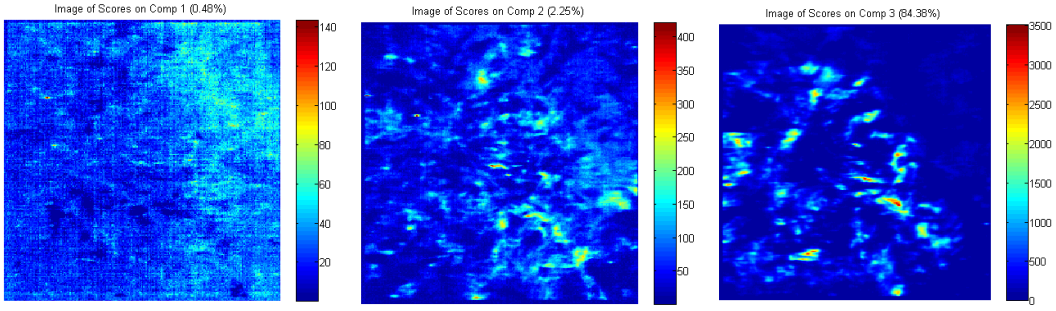

(a) Comp. 1 **(b)** Comp. 2 **(c)** Comp. 3

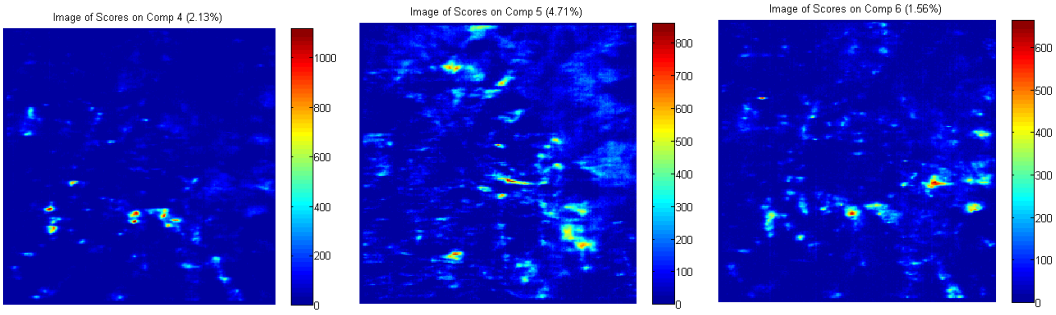

(d) Comp. 4 **(e)** Comp. 5 **(f)** Comp. 6

Fig. E.19

E.3 FS8-015, reference wafer

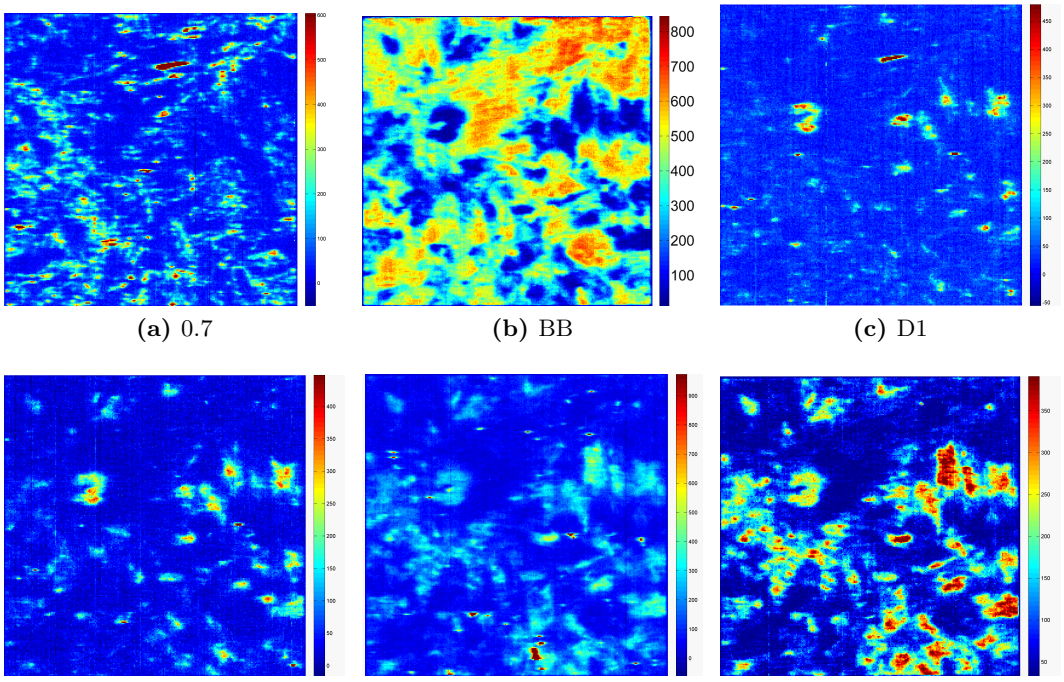

(a) 0.7 **(b)** BB **(c)** D1

(d) D2 **(e)** D3 **(f)** D4

Fig. E.21

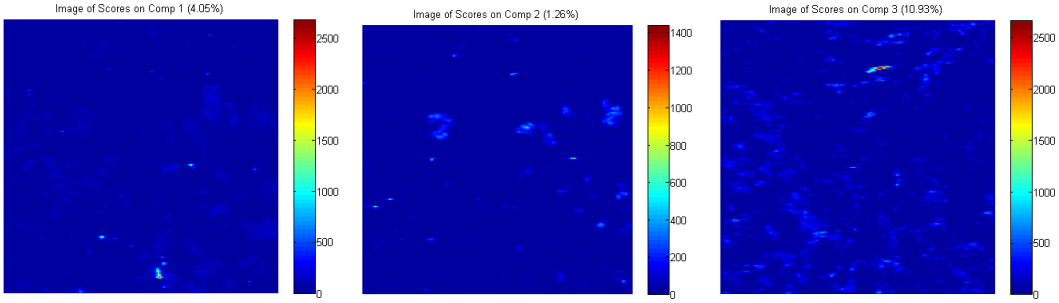

(a) Comp. 1

(b) Comp. 2

(c) Comp. 3

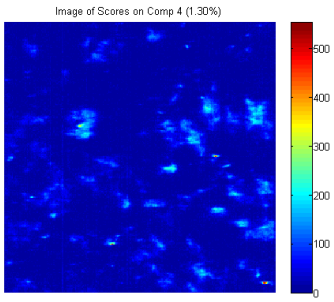

(d) Comp. 4

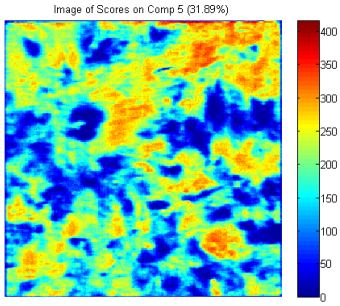

(e) Comp. 5

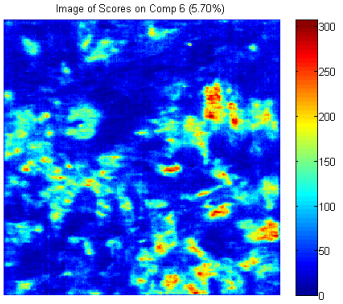

(f) Comp. 6

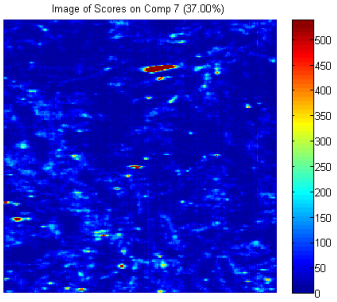

(g) Comp. 7

Fig. E.22

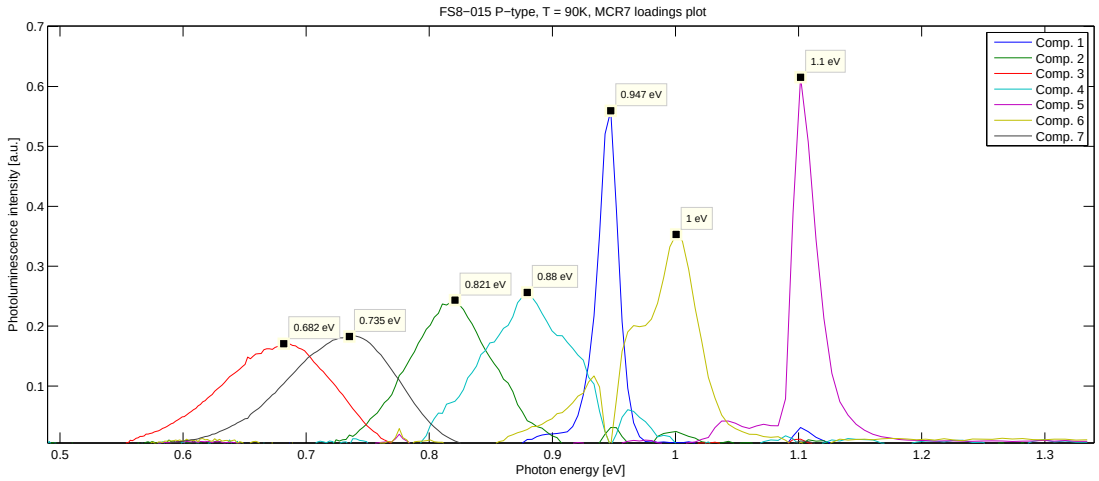
FS8−015 P−type, T = 90K, MCR7 loadings plot
Photoluminescence intensity [a.u.]
Photon energy [eV]
0.682 eV
0.735 eV
0.821 eV
0.88 eV
0.947 eV
1 eV
1.1 eV
Comp. 1
Comp. 2
Comp. 3
Comp. 4
Comp. 5
Comp. 6
Comp. 7

Fig. E.23

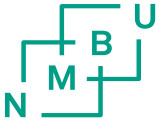

Norwegian University
of Life Sciences

Postboks 5003
NO-1432 Ås, Norway
+47 67 23 00 00
www.nmbu.no